University of Zurich[UZH]

Probing parity violations with multi-messenger observations of gravitational-wave transients

14th July 2021

Julia Stark

Master Thesis

Supervision: Dr. Maria Haney, Dr. Eleanor Hamilton

Group of Prof. Dr. Philippe Jetzer

Department of Physics
University of Zurich

Abstract

Gravitational parity violation induces an enhancement or suppression of the right- versus left-handed polarizations of gravitational-waves, called amplitude birefringence. In gravitational-wave signals from compact object binaries, this effect leads to a change in the apparent orientation of the binary system. The apparent change in the inclination angle could be used to probe amplitude birefringence. We investigate this phenomenon in the context of multi-messenger observations of gravitational-waves and electromagnetic signals from binary mergers. We estimate the strength of birefringence for observable effects and pursue a Fisher information analysis to make more general statements on the mesurability of birefringence. In particular, with the event GW170817, we are able to place an upper bound $\kappa < 20.2$ Gpc^{-1} on a parameter characterizing the strength of amplitude birefringence. Furthermore we show estimates of an upper bound on a Chern-Simons length scale depending on the comoving distance to the source and the signal-to-noise ratio.

Acknowledgments

I am grateful for the opportunity to pursue my Master thesis in the exciting field of gravitational-wave astronomy. In this regard I would like to thank Prof. Dr. Philippe Jetzer for his appreciated teachings on General Relativity and gravitational-waves, as well as on other subjects during my Bachelor and Master studies. I am thankful for the opportunity to write my thesis in his research group. Especially, I would like to thank my supervisors Dr. Maria Haney and Dr. Eleanor Hamilton for their support and insightful feedback during this project. I would also like to thank Michael Ebersold for helpful discussions and answers and Dr. Shubhanshu Tiwari for providing useful comments.

Contents

Introduction

Gravitational-waves are cosmic ripples in space-time produced in circumstances with extreme conditions − the strongest gravitational fields, densest celestial bodies and highest energy scales in physics. The strongest gravitational-waves are caused by some of the most violent and energetic processes in the universe such as supernovae or collisions of black holes or neutron stars. Albert Einstein predicted the existence of gravitational-waves in his general theory of relativity in 1916. His theory predicts that accelerated masses, such as black holes or neutron stars orbiting each other, would disrupt space-time in such a way that waves would propagate away from the source at the speed of light. These gravitational-waves (GWs) encode information about their origins and the nature of gravity itself. The first direct detection of GWs was achieved by LIGO in 2015 [1], when a transient GW signal generated by two colliding black holes 1.3 billion light-years away was observed. Subsequent detections of GWs by the LIGO-Virgo scientific collaboration have now led to the first confirmations of Einstein's theory in *extreme gravity* [2, 3], where gravity is strong and dynamical. Observations of GWs provide an excellent opportunity to test general relativity (GR) and alternative theories of gravity in this extreme gravity regime.

In this thesis, we will focus on testing the parity symmetry in gravity with GWs from compact object binaries. In Chapter 1 we will derive the parity-violating gravitational-waveform with parametrized deviations from GR in the framework of effective field theory. Parity violation has two main effects on the propagation of GWs, namely amplitude and velocity birefringence. We will further focus on amplitude birefringence, which causes different damping rates for the right- and left-handed polarization modes during propagation. This effect can be interpreted as a change in the apparent inclination angle of the binary. As put by Alexander et al. [4]: *In the same way that we say that the curvature of spacetime "bends" light passing close to strongly gravitating bodies we may say that the effect of the amplitude correction is to "rotate" the apparent inclination angle of the binary system's orbital angular momentum axis either toward or away from us.* We will explore this effect in Chapter 2 with a formalism that allows us to relate the apparent change in inclination to a parameter that can be used to constrain parity violating effects. A difference between the apparent inclination angle, called *effective inclination*, as is is seen by GW detectors and the actual *true inclination* as it could be inferred from an electromagnetic (EM) counterpart of binary mergers could in principle be observed when parity is violated. In order to understand in which circumstances it is possible to measure the inclination of a binary merger electromagnetically − and thus independent of the GW parameter estimation − we will review the main aspects of EM counterparts of compact binary mergers in Chapter 3. In Chapter 4 we will discuss the measurement of binary inclination angles via EM or GW signals. Then we will review the basics of GW data analysis in Chapter 5, in particular we consider Fisher information to estimate the measurement accuracy of binary parameters.

In the second part of this thesis, we will first estimate how large the birefringence effect on GWs would need to be in order to produce observable differences in the effective and true inclination in Chapter 6. Then, in Chapter 7, we will use Fisher information to study more systematically estimations of the parameter characterizing the strength of amplitude birefringence.

Definitions

The *total inclination* of the binary is defined as the angle θ_{JN} between the system's total angular momentum $\boldsymbol{J}$ and the line of sight $\boldsymbol{N}$, whereas the *orbital inclination*, or just *inclination*, ι defines the angle between the orbital angular momentum $\boldsymbol{L}$ and $\boldsymbol{N}$. We define the *viewing angle* of the binary as $\Theta \equiv \min(\iota, 180^\circ - \iota)$. Throughout this thesis, the metric convention is chosen as $(-,+,+,+)$ and we use units with $c = \hbar = 1$.

Part I

Theory and methods

1 Gravitational parity violation

Symmetries are fundamental to all laws of modern physics. Therefore, it is important to experimentally test the conservation of these symmetries. Parity symmetry implies the invariance of physical laws under the reversal of spatial coordinates. This means that a directional flipping to the right or left does not change the laws of physics. It is well known that parity is conserved for the strong and electromagnetic interactions but is broken in weak interactions [5], first discovered in beta-decay of cobalt-60 [6, 7]. Gravitational parity is conserved in Einstein's theory of general relativity. Nevertheless, in some fundamental theories of gravity, such as string theory and loop quantum gravity, parity violation in the high energy regime is inevitable [8]. Various parity violating theories of gravity have been proposed for different motivations, including Chern-Simons gravity, ghost-free scalar-tensor gravity, the symmetric teleparallel equivalence of GR theory and Hořava-Lifshitz gravity. Thus it is necessary to experimentally test the parity symmetry in the gravity sector.

1.1 Gravitational-waves in parity violating gravities

Our aim is to investigate possible imprints of parity violations in gravitational-waves. We want to derive a generalized waveform generated by compact binaries in the presence of parity violation using the effective field theory (EFT) formalism. Working within an EFT formalism ensures that the approximate theory is well-posed and that the corrections to GR are small [9]. EFT provides a systematic framework to encode different modifications to an existing theory and thus to test a range of modified gravity theories at once [5].

In particular, we assume that all modifications to the waveform arise from parity violating propagation effects and ignore the generation effects mainly causing a modified energy loss, inspiral rate and chirping rate of the binary. This assumption is justified because the generation effects occur on a radiation-reaction time scale, which is much smaller than the GW travelling time, making their modifications to the waveform negligible [10].

To investigate possible propagation effects due to parity violation, we consider the perturbation theory of the gravitational field and assume the gravitational-waves to propagate in a homogeneous and isotropic background. In a flat Friedmann-Robertson-Walker universe the line element can be written as

$$ds^2 = a^2(\tau)\left[-d\tau^2 + (\delta_{ij} + h_{ij})dx^i dx^j\right], \tag{1.1}$$

where the tensor perturbations h_{ij} of the metric represents the GW. This expression is written in terms of the conformal time τ which relates to the cosmic time t by $dt = ad\tau$, and $a(\tau)$ being the conformal scale factor of the universe with the present value $a_0 = 1$ and x^i the spatial coordinates. The spatial part of the metric is written as

$$g_{ij} = a^2(\tau)(\delta_{ij} + h_{ij})(\tau, x^i). \tag{1.2}$$

The metric perturbations are taken to be transverse and traceless, i.e. $\partial^i h_{ij} = 0$ and $\delta^{ij} h_{ij} = 0$.

We consider parity violating gravities with the action of the form [11]

$$S = \frac{1}{16\pi G}\int d\tau d^3x a^4(\tau)\left[\mathcal{L}_{\rm GR}+\mathcal{L}_{\rm PV}+\mathcal{L}_{\rm other}\right], \tag{1.3}$$

where $\mathcal{L}_{\rm GR}$ is the Einstein-Hilbert term with the Ricci scalar R and $\mathcal{L}_{\rm PV}$ is the parity violating Lagrangian, which consists of a number of terms in the specific models. $\mathcal{L}_{\rm other}$ is the Lagrangian for other matter fields, scalar fields and modification terms of gravity which are not relevant to parity violation. $\mathcal{L}_{\rm other}$ will therefore not be considered in what follows. For a detailed derivation and discussion of the effective action that incorporates gravitational parity violation consider [10, 12].

In order to derive the equation of motion for the GWs in vacuum, we first need to substitute the metric perturbation into the action and expand it to second order in h_{ij} to obtain the quadratic action [12]

$$S^{(2)} = \frac{1}{16\pi G}\int d\tau d^3x a^4(\tau)\left[\mathcal{L}^{(2)}_{\rm GR}+\mathcal{L}^{(2)}_{\rm PV}\right], \tag{1.4}$$

where

$$\begin{aligned}\mathcal{L}^{(2)}_{\rm GR} &= \frac{1}{4a^2}\left[(h'_{ij})^2-(\partial_k h_{ij})^2\right],\\ \mathcal{L}^{(2)}_{\rm PV} &= \frac{1}{4a^2}\left[\frac{c_1(\tau)}{a}\epsilon^{ijk}h'_{il}\partial_j h'_{kl}+\frac{c_2(\tau)}{a}\epsilon^{ijk}h_{il}\partial^2 h_{il}\partial_j h_{kl}\right].\end{aligned} \tag{1.5}$$

A *prime* denotes the derivative with respect to the conformal time τ and ∂_j the derivative with respect to spatial coordinates. ϵ^{ijk} is the Levi-Civita tensor. EFT suggests that the leading order contribution from parity violation in $\mathcal{L}^{(2)}_{\rm PV}$ comes from terms with three derivatives. The coefficients c_1 and c_2 are functions of time which are determined by the specific models of modified gravity. This effective field theory with leading order extensions to GR can describe the GW propagation effect with parity violation for all existing modified gravity models [12, 11].

By varying the action with respect to h_{ij}, the field equation of motion for h_{ij} is obtained [12]

$$h''_{ij}+2\mathcal{H}h'_{ij}-\partial^2 h_{ij}+\frac{\epsilon^{ilk}}{aM_{\rm PV}}\partial_l\left[c_1 h''_{jk}+(\mathcal{H}c_1+c'_1)h'_{jk}-c_2\partial^2 h_{jk}\right]=0, \tag{1.6}$$

where $\mathcal{H}\equiv a'/a$.

When working with parity violation, it is convenient to decompose the GWs into circular polarization modes. One can decompose h_{ij} into different polarization states as follows [9]

$$h_{ij}=\sum_P h_P e^P_{ij}, \tag{1.7}$$

where P denotes the polarization states and e^P_{ij} is the polarization basis. A common choice is the "plus" + and "cross" × polarization basis, but circular polarizations are more useful in the context of parity violation. Thus we choose $P = A = (R, L)$ corresponding to the right- and left-handed modes respectively. The circular polarization bases are written in terms of the + and × mode polarization tensors e^+_{ij} and $e^\times_{ij}$ as [13]

$$e^R_{ij} = \frac{e^+_{ij} + ie^\times_{ij}}{\sqrt{2}}, \qquad e^L_{ij} = \frac{e^+_{ij} - ie^\times_{ij}}{\sqrt{2}}. \tag{1.8}$$

Similarly one can write h_A in terms of $h_{+,\times}$ as

$$h_R = \frac{h_+ - ih_\times}{\sqrt{2}}, \qquad h_L = \frac{h_+ + ih_\times}{\sqrt{2}}. \tag{1.9}$$

To study the evolution of h_{ij} in Equation (1.6), we expand it over spatial Fourier harmonics [11, 12]

$$h_{ij}(\tau, x^i) = \sum_{A=R,L} \int \frac{d^3k}{(2\pi)^3} h_A(\tau, k^i) e^{ik_i x^i} e^A_{ij}(k^i). \tag{1.10}$$

The propagation equation of the left- and right-handed modes are decoupled and can be cast into the form [12]

$$h''_A + (2 + \nu_A)\mathcal{H}h'_A + (1 + \mu_A)k^2 h_A = 0, \tag{1.11}$$

where k is the wave number and

$$\nu_A = \frac{\rho_A k(c_1\mathcal{H} - c_1')/(a\mathcal{H})}{1 - \rho_A k c_1/a} \simeq \rho_A k(c_1 - c_1'/\mathcal{H})/a, \tag{1.12}$$

$$\mu_A = \frac{\rho_A k(c_1 - c_2)/a}{1 - \rho_A k c_1/a} \simeq \rho_A k(c_1 - c_2)/a, \tag{1.13}$$

with $\rho_R = +1$ and $\rho_L = -1$. The approximations in ν_A and μ_A are based on the assumption that $kc_1 \ll 1$ and $kc_2 \ll 1$ which is discussed in [12].

The effects of the parity violating terms are fully characterized by the two parameters μ_A and ν_A. The parameter μ_A modifies the conventional dispersion relation and determines the speed of the gravitational-waves, which leads to different velocities of right- and left-handed circular polarizations, resulting in different arrival times of the two modes. This phenomenon is called *velocity birefringence*.

The parameter ν_A changes the friction term in the GW propagation equation, which gives rise to an amplitude modification to the gravitational-waveform, such that the amplitude of the right-hand circular polarization increases during propagation while the amplitude of the left-hand polarization decreases or vice-versa. This effect is called *amplitude birefringence*.

It is interesting to note that in Chern-Simons (CS) modified gravity there are no modifications on the velocity of GWs but the parity violation only affects the amplitude. However, in the ghost-free parity violating gravities and other theories both velocity and amplitude birefringence effects exist during the propagation of GWs. A thorough review of general parity violating gravities is provided in [11].

As demonstrated by [12, 11], the parity-violating waveform in Fourier domain can be expressed as

$$h_A = h^{\rm GR}_A \delta h_A e^{i\delta\Psi_A}, \tag{1.14}$$

with $h_A^{\rm GR}$ being the GR waveform and δh_A and $\delta\Psi_A$ the amplitude and phase corrections due to parity violating effects.

As demonstrated in [14], a modified dispersion relation leads to a GW phase correction[1]

$$\delta\Psi_A = (\pi f)^2 \rho_A \int_{t_e}^{t_0} \frac{c_1 - c_2}{a^2} dt, \tag{1.15}$$

where f is the GW frequency at the detector.

The amplitude modification is given by [12]

$$\delta h_A = \exp\left(-\frac{1}{2}\int_{\tau_e}^{\tau_0} \mathcal{H}\nu_A d\tau\right) = \exp\left(-\frac{\rho_A k}{2}\int_{\tau_e}^{\tau_0} \frac{(c_1\mathcal{H} - c_1')}{a} d\tau\right). \tag{1.16}$$

From this we see clearly that the effect of gravitational parity violation is an enhancement/suppression of the right/left-polarized content of a GW. By mapping from the circular polarization bases to the linear $(+,\times)$ basis, using $h_+ = (h_R + h_L)/\sqrt{2}$ and $h_\times = i(h_R - h_L)/\sqrt{2}$, one can observe a mixing of the $(+,\times)$ polarisations that is enhanced upon propagation [10]. Linearizing about the GR solution, using $\delta h_A = 1 + \rho_A \delta\tilde{h}$ and $h_A = h_A^{\rm GR}(1 + \rho_A\delta\tilde{h})e^{i\rho_A\delta\tilde{\Psi}}$, we find [5]

$$h_+ = h_+^{\rm GR} - h_\times^{\rm GR}(i\delta\tilde{h} - \delta\tilde{\Psi}), \qquad h_\times = h_\times^{\rm GR} + h_+^{\rm GR}(i\delta\tilde{h} - \delta\tilde{\Psi}). \tag{1.17}$$

This *polarization mixing* is the main parity violating propagation effect, meaning that the initial polarization state is not conserved under propagation.

1.2 General gravitational-wave amplitude birefringence

Let us now focus on amplitude modifications in the waveform arising from parity violations. We can write the amplitude correction factor given in Equation (1.16) in the following form

$$\delta h_R = \exp\left(\pi f\tilde{\kappa}\right), \qquad \delta h_L = \exp\left(-\pi f\tilde{\kappa}\right), \tag{1.18}$$

where we used that $k = 2\pi f$, with f being the frequency of the gravitational-wave. The parameter $\tilde{\kappa}$ can be interpreted as an opacity parameter that characterizes the strength of amplitude birefringence. This parameter can be mapped on to various beyond-GR theories. Comparing with Equation (1.16) we find that

$$\tilde{\kappa} = -\int_{\tau_e}^{\tau_0} \frac{(c_1\mathcal{H} - c_1')}{a} d\tau. \tag{1.19}$$

The coefficients c_1 for some modified gravity models are presented in [11].

By experimentally constraining $\tilde{\kappa}$ in gravitational-waves it is possible to generally probe amplitude birefringence but also to place constraints on specific parameters in modified gravity

[1] A more general parametrized dispersion relation is constructed in [14] that reproduces a range of known Lorentz-violating predictions of modified gravity theories. Their impact on the propagation of GWs is studied and the GW phase corrections are given in their equations $28 - 32$. These phase corrections to GR are used by the LIGO and Virgo collaboration in their parametrized tests of gravitational-wave propagation in [2].

theories.

Assuming that $|\pi f\tilde{\kappa}| \ll 1$, which is justified in the effective field theory treatment, we can linearize about the GR solution to obtain $\delta h_A = 1 + \rho_A \pi f\tilde{\kappa}$ and $h_A = h_A^{\rm GR}(1 + \rho_A \pi f\tilde{\kappa})$. Now the plus and cross polarizations can be written as

$$h_+ = h_+^{\rm GR} - h_\times^{\rm GR} i\pi f\tilde{\kappa}, \qquad h_\times = h_\times^{\rm GR} + h_+^{\rm GR} i\pi f\tilde{\kappa}. \tag{1.20}$$

1.3 Amplitude birefringence in Chern-Simons gravity

Chern-Simons modified gravity is an effective extension of general relativity that incorporates leading-order gravitational parity violation. The theory of generic parity violation as it has been studied in 1.1 has been shown to reduce to dynamical Chern-Simons gravity [10, 15, 8].

In CS gravity, the Einstein-Hilbert action of GR is modified through the inclusion of a scalar field θ coupled to a term quadratic in space-time curvature. This leads to an exponential enhancement and suppression of the GW amplitudes of the right versus left circularly-polarized modes during propagation. The strength of this amplitude birefringence is governed by the properties of the CS scalar field [8]. The amplitude correction we derived in Equation (1.16) in the case of CS gravity is usually expressed as

$$\delta h_A = \exp\left(\frac{\rho_A k(t)}{H_0}\zeta(\theta)\right), \tag{1.21}$$

with $k(t)$ being the wavenumber for a given Fourier propagating mode and ζ is a dimensionless function of the integrated history of the CS scalar field. H_0 is the Hubble constant.

The function $\zeta(\theta)$ has been calculated in [8] for a matter dominated cosmological model, in which $a(\eta) = a_0\eta^2$, in terms of dimensionless conformal time η (with the convention of $\eta = 1$ corresponding to the present day) as

$$\zeta(\theta) = H_0^2 \int_\eta^1 \left[\frac{1}{4}\theta''(\eta) - \frac{1}{\eta}\theta'(\eta)\right] \frac{d\eta}{\eta^4}. \tag{1.22}$$

For GW sources at large redshifts $z \lesssim 30$, to which space-based detectors like LISA will be sensitive, the GWs travel over cosmological distances and can well be described in a matter dominated cosmological model [4].

In a dark energy dominated universe with scale factor $a(t) = a_0 e^{H_0 t}$, ζ has been computed by [16] to be

$$\zeta(\theta) = \frac{H_0^2}{2} \int_\eta^1 \left[\eta\theta''(\eta) - 2\eta\theta'(\eta)\right] d\eta. \tag{1.23}$$

This would be applicable to GW sources in the local universe, such as those found by LIGO at redshifts $z \lesssim 1$, where the universe is dark energy dominated.

1.4 Chern-Simons length scale of non-dynamical CS gravity

In *non-dynamical* CS gravity, the scalar field θ does not evolve dynamically, but is instead externally prescribed. Within this non-dynamical model, there is a particular choice of θ that has been extensively used; the *canonical* profile [15, 8]

$$\theta = \frac{t}{\mu}, \tag{1.24}$$

where μ is some mass scale with units $[\mu] = L^{-1}$. Note that this field profile is isotropic and that for large μ we recover GR.

The CS length scale for this profile can be defined as [16]

$$l_0 \equiv \frac{1}{\mu}. \tag{1.25}$$

With this field profile, $\zeta(\theta)$ can be computed for a dark energy dominated universe given in Equation (1.22). Using [16]

$$\theta' = \frac{d\theta}{d\eta} = \frac{d\theta}{dt}\frac{dt}{d\eta}, \qquad \text{with} \qquad \frac{dt}{d\eta} = a(\eta) = -\frac{1}{H_0\eta}, \tag{1.26}$$

we find that

$$\theta' = -\frac{l_0}{H_0\eta}, \qquad \theta'' = \frac{l_0}{H_0\eta^2}. \tag{1.27}$$

Inserting this into Equation (1.22) and evaluating the integral we find that [16]

$$\zeta(\theta) = \frac{3H_0 l_0}{2c}(1-\eta) = \frac{3H_0^2 d_C l_0}{2c}. \tag{1.28}$$

Here we have reintroduced a factor of c and set $(1-\eta)\frac{c}{H_0} \sim d_C$, with d_C being the comoving distance[2] to the source.

The opacity parameter $\tilde{\kappa}$ defined in Equation (1.18) can be mapped to the function $\zeta(\theta)$ as

$$\tilde{\kappa} = \frac{2}{H_0}\zeta(\theta). \tag{1.29}$$

Therefore, by measuring $\tilde{\kappa}$, the Chern-Simons length scale for a canonical θ profile can be computed as

$$l_0 = \frac{\tilde{\kappa}c^2}{3d_C H_0}. \tag{1.30}$$

An experimental bound on $\tilde{\kappa}$ thus translates to a bound on l_0.

[2]Recall the definitions of the comoving distance $d_C = c\int_{t_e}^{t_0}\frac{dt'}{a(t')}$ and the conformal time $\tau_e = \int_0^{t_e}\frac{dt'}{a(t')}$ with t_e and t_0 being the time at emission and the current cosmic time respectively and $t = 0$ corresponding to the time at the Big Bang [17]. For a treatment of our problem using units of dimensionless conformal time, see Appendix C of [16].

2 A formalism for gravitational-wave amplitude birefringence

We have seen in the previous chapter that amplitude birefringence affects GWs when propagating from the source to the detector. The amplitudes of right versus left polarized modes are exponentially enhanced or suppressed during propagation. Following Okounkova et al. [16], the strength of amplitude birefringence can be expressed in terms of an opacity κ, while the frequency dependency is ignored. In this formalism, it is assumed that the wavenumber $k(t)$ covers a narrow frequency range and thus can be approximated by a typical value in this range $k(t) \sim k = 2\pi f$, with f being a frequency value in the region of greatest sensitivity of the GW detector.

In this formalism, the circular polarizations of GWs can be written as

$$h_R = h_R^{\mathrm{GR}} e^{-\kappa d_C}, \qquad h_L = h_L^{\mathrm{GR}} e^{\kappa d_C}. \tag{2.1}$$

Here, d_C is the comoving distance to the source (in units of length), which is connected to the luminosity distance d_L by $d_C = d_L/(1+z)$, where z is the redshift. The opacity κ has units of inverse length and for $\kappa = 0$, GR is recovered. Beyond-GR effects have to be small enough for an effective field theory treatment to be valid. Therefore, the assumption $|\kappa d_C| \ll 1$ is necessary.

Note the difference to the formalism presented in Chapter 1.2, where the amplitude correction factor is given by $\delta h_A = \exp(\rho_A \pi f \tilde{\kappa})$. Here on the other hand, the frequency is assumed to be constant and $\delta h_A = \exp(-\rho_A \kappa d_C)$. The parameters κ and $\tilde{\kappa}$ can be related by assuming the frequency to be constant as

$$\kappa d_C = -\tilde{\kappa} \pi f. \tag{2.2}$$

2.1 Effective inclination angle

Expressions for the gravitational-wave strain h for right and left circularly polarized modes in terms of the plus and cross polarizations have been given previously in Equation (1.9). In GR, for non precessing inspirals the ratio of h_R to h_L is purely a function of the inclination angle ι of the binary for the dominant angular mode (2,$\pm$2) and all higher modes with $l = |m|$, namely[1]

$$\left(\frac{h_R}{h_L}\right)_{\mathrm{GR}} = \left(\frac{1+\cos\iota}{1-\cos\iota}\right)^2. \tag{2.3}$$

The geometry of a system is exactly *face-on* when $\cos\iota = 1$ and the power is purely in the right circular polarization h_R. A system is exactly *face-off* when $\cos\iota = -1$ and the polarization is purely left circular h_L. A binary system is also called face-on, when $\cos\iota > 0$, i.e. $\iota < \pi/2$ and face-off, when $\cos\iota < 0$, i.e. $\iota > \pi/2$.

In the presence of amplitude birefringence, we have

[1] See Appendix A for a derivation and generalizations.

$$\left(\frac{h_R}{h_L}\right)_{\text{biref}} = \left(\frac{h_R}{h_L}\right)_{\text{GR}} \frac{e^{-\kappa d_C}}{e^{\kappa d_C}} = \left(\frac{1+\cos\iota}{1-\cos\iota}\right)^2 e^{-2\kappa d_C}. \tag{2.4}$$

A traditional GW parameter estimation based on GR would observe some *effective inclination angle* ι_{eff} because of the additional exponential factor in Equation (2.4)

$$\left(\frac{h_R}{h_L}\right)_{\text{biref}} = \left(\frac{1+\cos\iota_{\text{eff}}}{1-\cos\iota_{\text{eff}}}\right)^2. \tag{2.5}$$

Thus, we can write

$$\frac{1+\cos\iota_{\text{eff}}}{1-\cos\iota_{\text{eff}}} = \frac{1+\cos\iota}{1-\cos\iota} e^{-\kappa d_C}. \tag{2.6}$$

From a GW observational standpoint, amplitude birefringence effectively modifies the actual inclination angle, leading to an apparent inclination angle ι_{eff} that depends on the strength of the observed amplitude birefringence, given by κd_C. This interpretation of the amplitude birefringence correction as inducing an effective inclination angle should be interpreted with care when the actual inclination angle of the binary is close to 0 or π. In GR, the amplitude of the gravitational-wave is a maximum, when the inclination is 0 or π. Amplitude birefringence, however, leads to an enhancement or suppression of the amplitude depending on whether the wave is right- or left-circularly polarized. When the amplitude birefringence effect suppresses the GW amplitude, one can interpret this as an effective modification of the inclination angle away from the maximum. However, when the birefringence effect enhances the amplitude, there is no real apparent inclination angle that can mimic this effect, i.e. the effective angle would have to be imaginary [8].

With Equation (2.6), the opacity parameter κ corresponding to fixed true and observed effective inclination angles can be calculated as

$$\kappa = \frac{1}{d_C} \ln\left(\frac{(1+\cos\iota)(1-\cos\iota_{\text{eff}})}{(1-\cos\iota)(1+\cos\iota_{\text{eff}})}\right). \tag{2.7}$$

The inclination angle $\cos\iota_{\text{eff}}$ observed by GW parameter estimation as a function of the true inclination angle $\cos\iota$ and κ is given by

$$\cos\iota_{\text{eff}} = \frac{-(1-\cos\iota)e^{\kappa d_C} + (1+\cos\iota)}{(1-\cos\iota)e^{\kappa d_C} + (1+\cos\iota)}, \tag{2.8}$$

or, alternatively, the true inclination given by the effective inclination is

$$\cos\iota = \frac{-(1-\cos\iota_{\text{eff}}) + (1+\cos\iota_{\text{eff}})e^{\kappa d_C}}{(1-\cos\iota_{\text{eff}}) + (1+\cos\iota_{\text{eff}})e^{\kappa d_C}}. \tag{2.9}$$

For $\kappa > 0$, the effective inclination angle becomes larger than the true inclination angle and for $\kappa < 0$, it becomes smaller. The difference between the true and the effective inclination angle, $|\iota - \iota_{\text{eff}}|$, depends on the parameter κd_C. Figure 2.1 shows the behaviour of κd_C and ι_{eff} for different true inclinations. For larger viewing angles, $|\iota - \iota_{\text{eff}}|$ becomes larger, when keeping

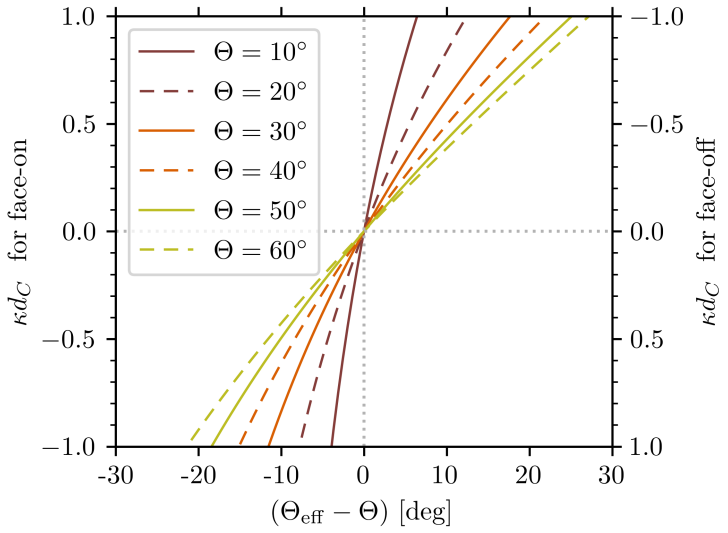

Figure 2.1: The parameter κd_C governing the strength of amplitude birefringence, as a function of the resulting change in the inclination angle. The different lines correspond to different true viewing angles Θ and on the x-axis we have the difference between the effective viewing angle $\Theta_{\rm eff}$ and the true viewing angle. For face-on systems, the viewing angle is identical to the inclination angle and the y-axis on the left applies for κd_C and for face-off systems, the viewing angle equals the subtraction of the inclination angle from 180°, and the y-axis on the right applies for κd_C.

$|\kappa d_C|$ the same. Thus, the observed effect of amplitude birefringence is more prominent at larger viewing angles. This behaviour can also be seen in Figure 2.2. The maximum of the allowed values of $|\iota - \iota_{\rm eff}|$ is largest for edge-on systems ($\iota \sim 90°$).

Thus, to obtain the best constraints on $|\kappa|$, the inclination angle of the binary should not be too small and the distance d_C should be as large as possible.

Compact binary mergers with coincident EM observations (e.g. gamma-ray bursts and afterglows) could allow for a determination of the distance to the source or the binary inclination angle that is independent from GW parameter estimation. Therefore, such EM-bright binary mergers can be used to investigate the effect of amplitude birefringence. The "true" inclination angle and distance can be obtained from EM observations and, while fixing this EM distance in a GW parameter estimation of the inclination angle[2], the effective inclination can be obtained. The difference between "true EM inclination" and "effective GW inclination" could be used to constrain the amplitude birefringence parameter κ.

In order to understand how the inclination of a binary can be measured entirely independent from the GW observation, we will have a look at electromagnetic counterparts of compact binary mergers and the information that can be extracted thereof in Chapter 3.

[2]In Chapter 4 we will discuss the degeneracy of the inclination angle and distance in GW signals. This degeneracy can be broken with an independent EM distance measurement, which leads to improved inclination constraints.

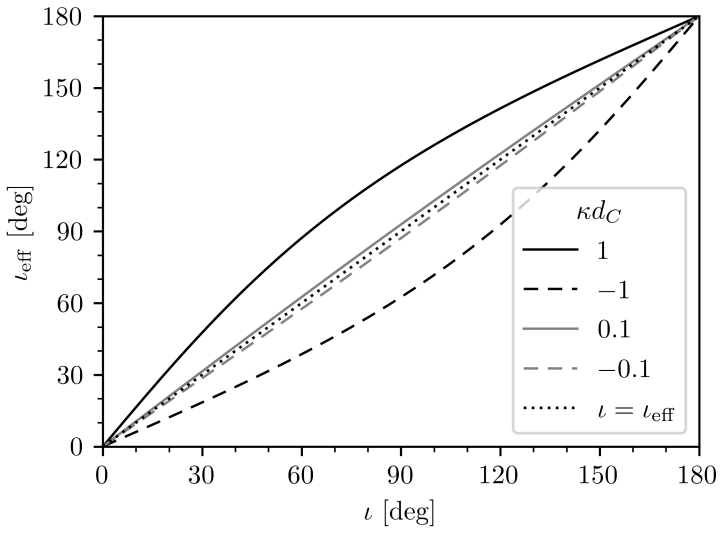

Figure 2.2: Effective inclination angle as a function of the true inclination angle with fixed κd_C. The allowed region with $|\kappa d_C| < 1$ lies between the black lines.

2.2 Effect on measurements of the Hubble constant with gravitational-waves

As an additional comment we will briefly discuss the effect of amplitude birefringence on the luminosity distance derived from GWs and how it translates to a determination of the Hubble constant.

Birefringence changes the amplitude of the signal measured at the detector and thus the inferred luminositiy distance to the source via[3]

$$\frac{d_{\rm L,eff}}{d_L} = 1 + \frac{\cos\iota_{\rm eff}(\cos^2\iota_{\rm eff} - 5)}{2(1+\cos^2\iota_{\rm eff})}\kappa d_C + \mathcal{O}(\kappa d_C)^2. \tag{2.10}$$

For a flat FLRW geometry, the luminosity distance can be written as [18]

$$d_L = \frac{1+z}{H_0}\int_0^z \frac{dz'}{E(z')}. \tag{2.11}$$

A determination of the Hubble constant H_0 using gravitational-waves from EM-bright binary mergers to measure the distance while fixing the inclination angle and redshift with an independent measurement from an EM counterpart has been discussed by several authors (e.g. [19, 20, 21]). Such a determination of the Hubble constant is discussed in the light of current tensions between the two measurements by the Planck cosmic microwave background and the SH0ES Cepheid-supernovae distance ladder surveys. It would offer an independent standard siren without the assumption of a cosmological model and independent of a cosmic distance ladder.

However, in the presence of amplitude birefringence the luminosity distance derived from gravitational-waves is affected. Thus, the derived Hubble constant $H_0^{\rm eff}$ can be altered. The

[3]For a derivation of this expression, see [16].

ratio of the effective Hubble constant to the "true" one can be written as

$$\frac{H_0^{\rm eff}}{H_0} = \frac{d_L}{d_{\rm L,eff}} \approx \left(1 + \frac{\cos\iota_{\rm eff}(\cos^2\iota_{\rm eff} - 5)}{2(1+\cos^2\iota_{\rm eff})}\kappa d_C\right)^{-1}. \tag{2.12}$$

This ratio as a function of the observed effective viewing angle for different values of κd_C is shown in Figures 2.3 and 2.4. The effect vanishes for edge-on systems and is largest for face-on systems and $\kappa > 0$ or face-off systems and $\kappa < 0$ at a viewing angle of $\sim 40°$.

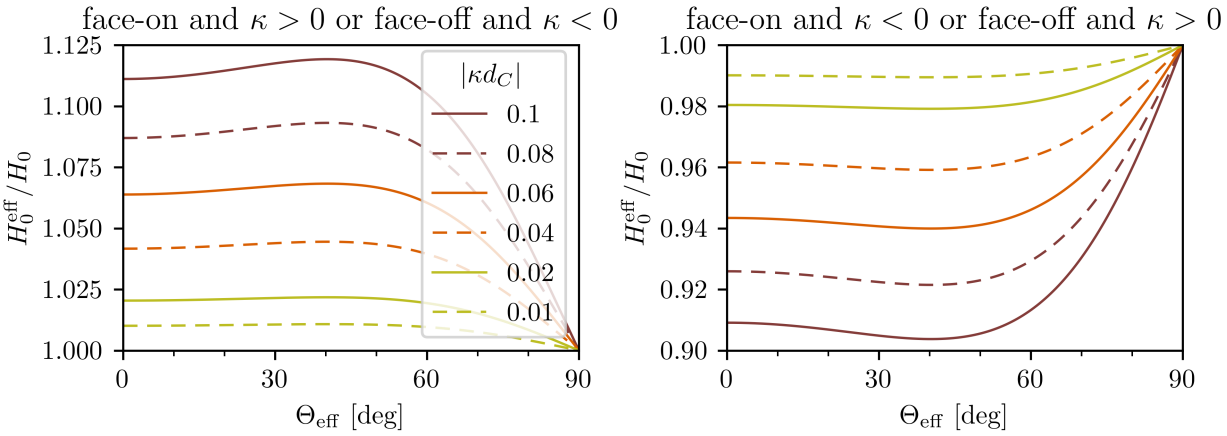

Figure 2.3: Amplitude birefringence effect on a Hubble constant determined from the luminosity distance measured with gravitational-waves, as a function of the effective viewing angle. For face-on systems, the effective inclination angle is identical to the effective viewing angle and for face-off systems, $\iota_{\rm eff} = 180° - \Theta_{\rm eff}$. Plotted for different values of $|\kappa d_C| < 0.1$.

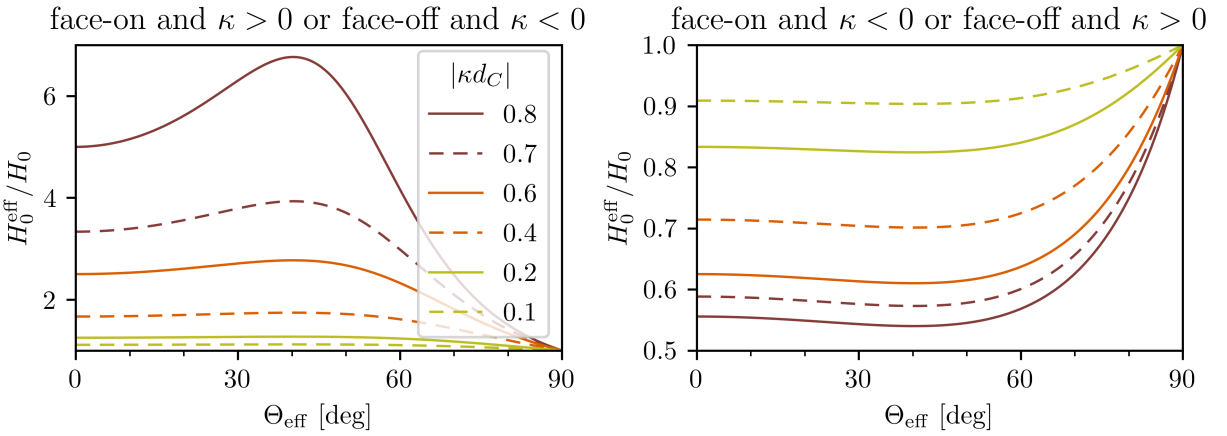

Figure 2.4: Same as in Figure 2.3 but for different values of $|\kappa d_C| > 0.1$.

3 Electromagnetic counterparts of compact binary mergers

Multi-messenger observations of compact binary mergers offer a unique opportunity to study a range of physical and astrophysical processes using two different and almost orthogonal probes – gravitational-waves and electromagnetic emission [21]. In particular, combining information from the electromagnetic counterpart and the GW signal leads to better estimations of various binary parameters. EM constraints on the distance and sky location of a binary merger can break degeneracies between different parameters in the GW parameter estimation. Additionally, it is possible to measure the inclination of a binary electromagnetically in binary neutron star (BNS or neutron star-black hole (NSBH) mergers, if a relativistic jet is created after the merger and if the afterglow light curve can be observed. The asymmetric masses in NSBH mergers further allow for better inclination constraints from GWs.

In this chapter we will present the theoretical background in order to understand how the inclination can be inferred from the EM counterpart of a compact binary merger. We first give an overview of the outflow from compact binary mergers and its EM emission and then focus more specifically on NSBH mergers. We will study the requirements for a NSBH merger to produce an EM counterpart and examine its parameter space. Finally we look at the detectability of an afterglow depending on the distance to the merger and its viewing angle.

3.1 Outflow from mergers and its electromagnetic emission

The main reference for this chapter is a review by Nakar [21], if not indicated otherwise.

A merger of a binary neutron star or a neutron star-black hole is expected to have sub-relativistic and relativistic outflow components. The three major sources of the sub-relativistic outflow are (i) tidal forces operating during the final stages of the inspiral and during the merger and ringdown, (ii) shocks driven by the collision between the two binary members in the case of a BNS, and (iii) winds from the accretion disk formed following the merger. All of these sources involve decompression of highly dense neutron rich material, leading to nucleosynthesis of r-process elements. The heavy nuclei formed in this process are not stable and therefore go through a chain of beta-decay, alpha-decay and nuclear fission on their way to stability. This radioactive decay provides a continuous source of heat that escapes as an ultraviolet, optical and infrared radiation detectable for weeks and even months. This radiation is often called *kilonova* (sometimes referred to as *macronova* in the literature) in the case of compact binary mergers. The subrelativistic ejecta interacts with the circum-merger medium and produces a radio remnant which may be detectable on a timescale of months to years. The properties of the sub-relativistic ejecta depend on the nature of the binary (i.e. BNS or NSBH), the spins and masses of the binary members, and the neutron star (NS) equation of state (EOS).

After the merger, some of the bound material settles into an accretion disk surrounding a rapidly rotating central object, which may be a highly magnetized neutron star (magnetar) or a black hole. In NSBH mergers the merged central object is a black hole (BH), where as in BNS mergers, the nature of the central object depends on the total binary mass and on the NS EOS. If the merged object is NS supported by rotation, it can collapse to a BH at any time. Both

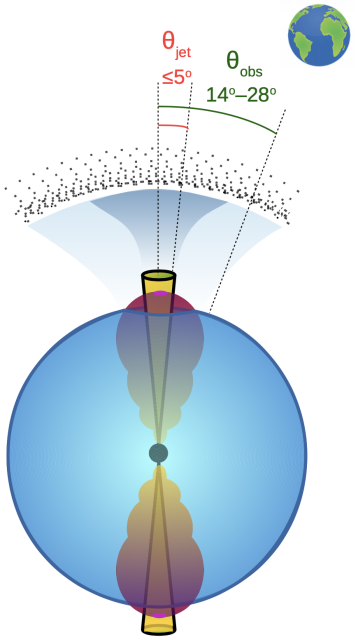

Figure 3.1: A schematic illustration showing the geometry of the relativistic jet that was launched following the BNS merger GW170817. The successful jet (yellow) drives a cocoon (red) through interaction with the dynamical ejecta (blue). This scenario is consistent with structured jet models. Shock-breakout of the jet from the ejecta likely produced the γ-ray signal and the interaction of the cocoon with the ISM produced the early-time afterglow emission (up to ~ 2 months post-merger). The late-time afterglow emission is produced by the interaction between the jet and the ISM. The total energy of the jet-cocoon is estimated to $10^{49} - 10^{50}$ erg (the isotropic-equivalent energy to $\gtrsim 10^{52}$ erg) and the density of the circum-merger environment to $10^{-4} - 5 \times 10^{-3}\mathrm{cm}^{-3}$. The jet has a narrow relativistic core with half-opening angle $\theta_{\rm jet} \lesssim 5^{\circ}$ pointing away from the Earth at a viewing angle angle $\theta_{\rm obs} \sim 20^{\circ}$. From Mooley et al. [24].

types of system - a rapidly rotating magnetar or a BH with a disk - are promising sources of ultra-relativistic jets, such as those present in gamma-ray bursts (GRBs). These jets constitute the relativistic outflow component expected in a compact binary merger.

Gamma-ray bursts are astrophysical transients with the defining feature being their non-repeating, non-periodic prompt γ-ray emission. Within their broad range of properties, GRBs can be separated into at least two sub-classes, short and long duration bursts [22]. GRBs are exceptionally luminous cosmological explosions. A long GRB progenitor is a massive, low metallicity star exploding due to core collapse. The GRB jet itself arises from rotation and can be launched through different scenarios [23]. Short gamma-ray bursts (sGRBs) are expected to be generated by BNS and NSBH mergers. This model is also supported by the detection of sGRB afterglows.

The jet launched by compact binary mergers must penetrate through the sub-relativistic ejecta covering the polar region, break out of the ejecta and release an intense burst of gamma-rays. During the following interaction of the jet with the circum-merger medium, i.e. the interstellar medium (ISM), the driven blast wave generates long lasting X-ray, optical and radio *afterglows*. The extremely bright emission from the jet can be seen to high redshifts, but only if the observer is placed within the opening angle of the jet. At large angles, the emission from the jet is too faint for detection due to relativistic beaming. Since sGRB jets are most likely narrow, only rarely are we expected to be able to see the jet directly in mergers that are detected by

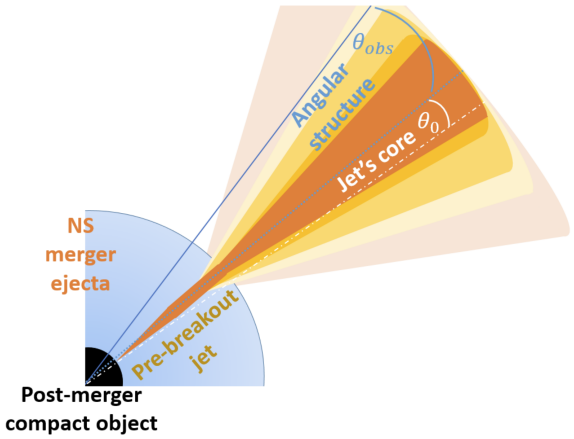

Figure 3.2: Schematic illustration of a structured jet with a strong angular profile beyond the jet core. An off-axis observer (located at an angle $\theta_{\rm obs}$) receives emission from the less energetic material outside the jet core. From Benjamini et al. [26].

their GW signal. Furthermore, the jet needs significant power to cross the entire sub-relativistic ejecta successfully. In some mergers, the jets will fail to do so and get choked within the ejecta. For this case of a choked jet, no direct detection by any observer is possible. Fortunately, also when the jet is directed away from us or when it is choked, it can leave an observable imprint.

As a relativistic jet propagates through the sub-relativistic material it inflates a high pressure bubble known as the *cocoon*. After braking out of the ejecta successfully, the jet together with the engulfing cocoon form an outflow, that is spread over an opening angle much wider than the opening angle of the jet itself. This entire outflow, known as the *jet-cocoon*, has mostly an angular structure. The narrowly collimated core along the jet axis has high isotropic-equivalent energy[1] and high Lorentz factor while outside of the core, the energy and Lorentz factor decrease with angle. A jet-cocoon outflow is a specific type of a *structured jet*, illustrated in Figure 3.2. Emission that might be observable at distances where GWs are detectable and that is generated over a wider angle is produced by the jet-cocoon via the following processes. Shock breakout (producing a short flash of γ-rays), cooling emission (X-ray, UV and optical), radioactively powered cocoon emission (possibly dominating the early macronova/kilonova emission) and interaction with the circum-merger medium (producing an X-ray, optical and radio afterglow possibly seen over a wide observing angle). Figure 3.1 illustrates the geometry of a jet-cocoon system.

A choked jet may also produce observable emission, if the jet deposits enough energy in the cocoon before being choked. Then the cocoon can break out of the sub-relativistic ejecta and produce emission via mostly the same processes as those of the successful jet-cocoon. However, the cocoon outflow in that case is only mildly relativistic and no sGRB is seen.

3.2 Neutron star-black hole mergers

In this chapter, we focus on the characteristics of NSBH mergers and mainly present the findings of Barbieri et al. [27, 28].

The final remnant in a NSBH merger is always a BH. For the fate of the NS however, there exist two different scenarios. Either the neutron star plunges entirely into the BH, or it

[1]The isotropic-equivalent energy is computed under the assumption of an isotropically emitting source. It depends on the angle between the jet axis and the line of sight and is obtained from the intrinsic jet structure (Lorentz factor and kinetic energy). For more details see [25].

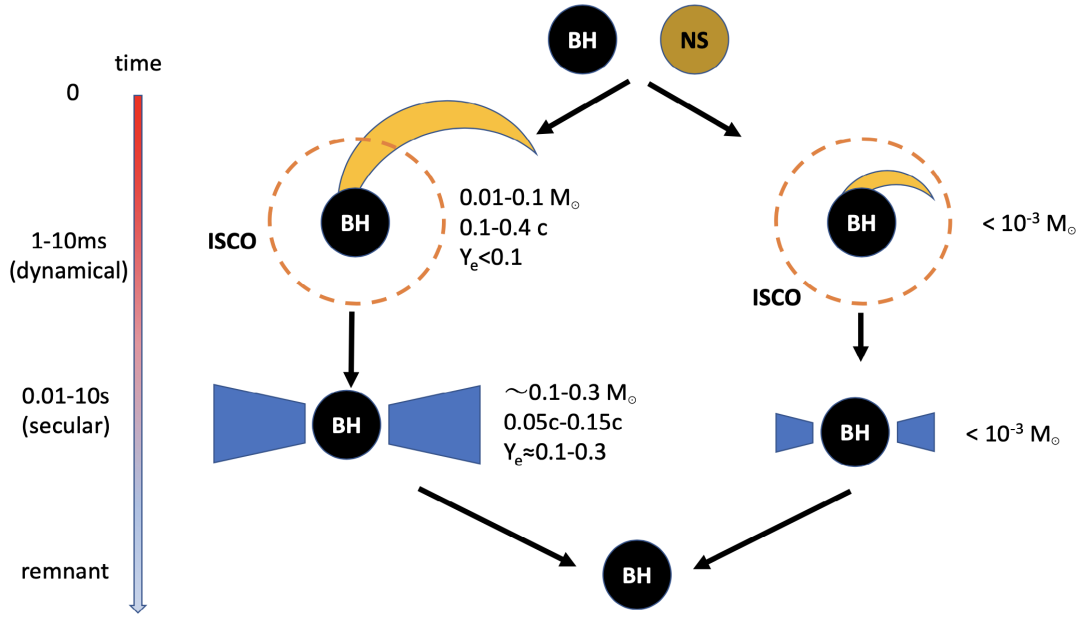

Figure 3.3: The two different scenarios (direct plunge of the NS on the right, tidal disruption outside the ISCO on the left) for a NSBH merger and its sub-relativistic ejecta. Dynamical ejecta are depicted above, the disc with its wind and secular ejecta below. A time scale for the ejection of dynamical and secular ejecta is given on the left. Rough estimates for the masses, velocities and electron fractions Y_e of the ejecta are listed. From Nakar [21].

is disrupted by the tidal field of the BH, leading to ejection of mass and the formation of an accretion disc around the BH [29]. Which scenario takes place depends on the relative position of the BH innermost stable circular orbit at a radius $R_{\rm ISCO}$ and the disruption radius $R_{\rm dis}$, at which the gravitational field of the BH induces the tidal disruption of the NS.

$R_{\rm ISCO}$ is determined by the BH mass $M_{\rm BH}$ and dimensionless spin parameter $\chi_{\rm BH} = cJ/GM_{\rm BH}^2$, where J is the angular momentum of the BH, c the speed of light and G Newton's constant. $R_{\rm ISCO}$ decreases for smaller BH masses or larger prograde spins. If $R_{\rm dis} < R_{\rm ISCO}$, the tidal disruption occurs too close to the BH leading to a direct plunge of the NS into the BH. No mass is left outside and no EM counterpart is expected. If instead $R_{\rm dis} > R_{\rm ISCO}$, the NS undergoes partial disruption, spreading neutron-rich matter in its surroundings. The tidal debris left outside of the remnant BH can be divided into two components: the gravitationally bound material forming an accretion disc, and the unbound part called dynamical ejecta. In this case with matter present outside the BH, EM emission is expected to emerge from a variety of processes.

These two evolutionary paths and the ejecta components of a NSBH merger are summarized in a sketch in Figure 3.3.

The fate of the neutron star depends on the NS tidal deformability $\Lambda_{\rm NS}$ and thus on the equation of state for nuclear matter inside the NS, on the BH and NS mass ratio $q = M_{\rm BH}/M_{\rm NS}$, and on the BH spin $\chi_{\rm BH}$. For a given NS mass, a "stiff" EOS leads to a larger NS radius, a lower compactness and consequently to larger tidal deformability $\Lambda_{\rm NS}$ compared to a "soft" EOS. For all existing physically motivated EOS, low mass NSs correspond to the largest values of tidal deformability. NSs never suffer a total tidal disruption. For one of the stiffest physically motivated EOS (MS1) the remaining mass outside the remnant BH is $\lesssim 40\%$ $M_{\rm NS}$, as found by [27]. Considering the likely more realistic SFHo EOS [30], the remaining mass outside is $\lesssim 32\%$ $M_{\rm NS}$. This EOS is compatible with nuclear and astrophysical constraints and it associates

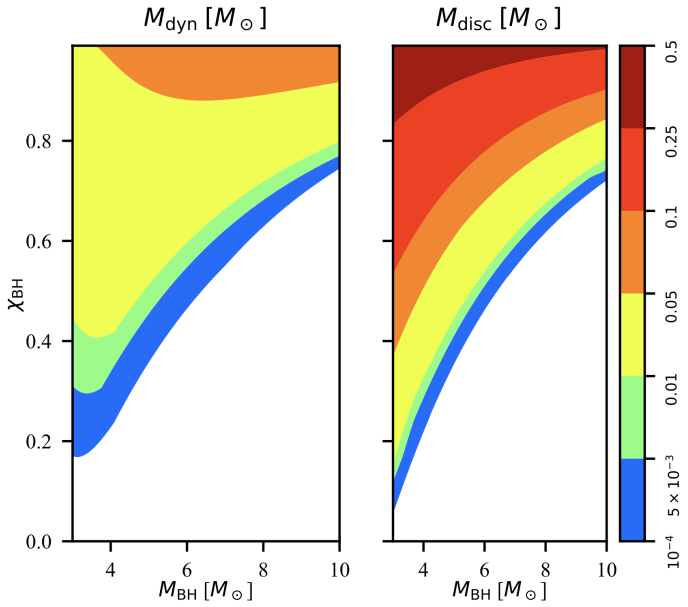

Figure 3.4: Masses of the dynamical ejecta (left) and disc (right) in the $M_{\rm BH}$ - $\chi_{\rm BH}$ parameter space assuming a NS with $M_{\rm NS} = 1.4\ M_\odot$ and $\Lambda_{\rm NS} = 330$. White regions correspond to parameters leading to no mass left outside of the BH, and therefore no EM counterpart. From Barbieri et al. [27].

to a NS of mass 1.4 $M_\odot$ a tidal deformability $\Lambda_{\rm NS} = 334$ and a radius of ~ 12 km. This radius is compatible with estimates of NS radii in the GW170817 signal analysis [31].

The NS is subject to partial disruption for larger values of $\Lambda_{\rm NS}$ (corresponding to stiffer EOS and low NS masses), low mass ratios q and high BH spins $\chi_{\rm BH}$. These quantities determine the production of dynamical ejecta and discs, which are essential for EM emission from NSBH binaries.

In Figure 3.4 it is shown how the production of dynamical ejecta and disc masses is affected by the BH mass and spin, as calculated by [27]. It is clear that, with fixed $M_{\rm NS}$ and $\Lambda_{\rm NS}$, more mass is left outside the BH for faster spinning and less massive BHs (i.e. smaller mass ratios q). White regions represent parameter combinations leading to a direct plunge of the NS, with no mass left outside the BH and thus no EM counterpart. The spin vector of the BH is assumed to be aligned with the orbital angular momentum such that the binary is non-precessing and the NS spin is neglected[2].

We have discussed that during the final phase of the inspiral, the NS can be partially disrupted, leaving gravitationally unbound material (dynamical ejecta) and bound material forming an accretion disc around the remnant BH created after the merger. Additional outflows are produced from the disc; the wind ejecta and the secular (viscous) ejecta. Furthermore, accretion onto the BH in the presence of magnetic fields can power the launch of a relativistic jet, potentially leading to the production of a short GRB. These outflows produce the EM counterparts. The sub-relativistic ejecta power the kilonova emission and the relativistic jet produces the GRB afterglow emission.

After the launch, the relativistic jet may in principle lose some energy upon interaction with the ambient medium, i.e. the other merger ejecta. However, it is assumed that the jet is launched

[2]The NS spin is expected to be negligible for reasons outlined in [27].

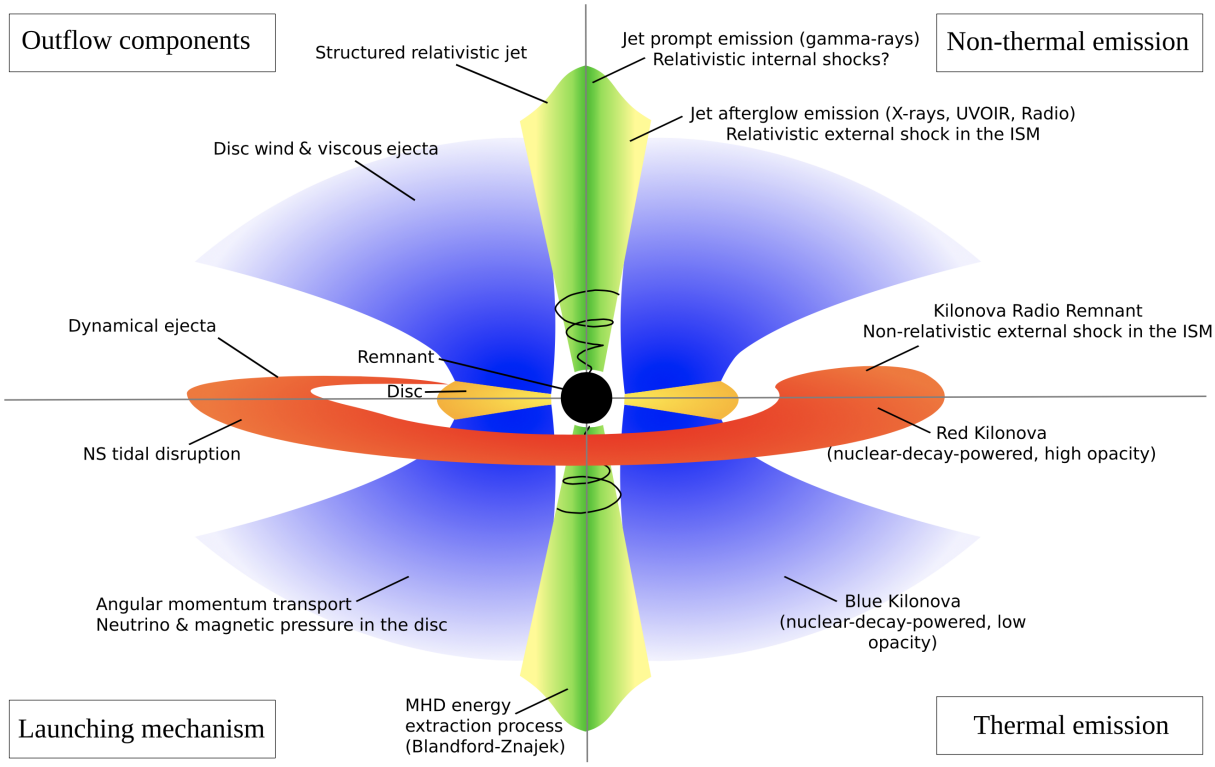

Figure 3.5: Illustration of the outflows and electromagnetic counterparts from a NSBH merger. The merger remnant, a spinning black hole, is surrounded by an accretion disc and the various types of outflows. The upper left quadrant of this sketch describes these outflow components and their launching mechanisms are stated in the lower left quadrant. The non-thermal and thermal emission components that arise from the outflows (either internally or upon interaction with the ISM) are listed in the upper and lower right quadrant respectively. From Barbieri et al. [28].

in the polar direction, perpendicularly to the accretion disc. Thus the jets propagates through very low density ejecta, since in NSBH mergers the dynamical ejecta lie close to the equatorial plane. This is due to the absence of shocks in the NSBH case. Shocks, as generated in the BNS case through the collision of the two stars, would produce a more isotropic ejection of matter. The wind ejecta is the only outflow emitted along the polar direction, but it contributes only very little mass. Therefore it can be assumed that the jet overcomes the ejecta and only spends a negligible fraction of its energy, without consequences on its structure.

Regardless of the jet launching mechanism, it is natural to expect an angular distribution of the kinetic energy per solid angle and of the Lorentz factor Γ in the jet. Indeed, as shown e.g. by [32], a jet launched by magneto hydrodynamic (MHD) energy extraction from a spinning BH naturally develops an angular structure of these two quantities. Both quantities decrease approximately exponentially with the angular distance from the axis of the jet.

Barbieri et al. [28] developed semi-analytical models to predict the properties of the EM counterparts of NSBH mergers. They present different light curves of the afterglow emission from the jet for two sets of parameters (BH mass and spin) and for three different viewing angles. The light curves for radio emission are shown in Figure 3.6. Brighter emission corresponds to lower BH mass and higher BH spin, as in these cases more massive ejecta are produced during the merger.

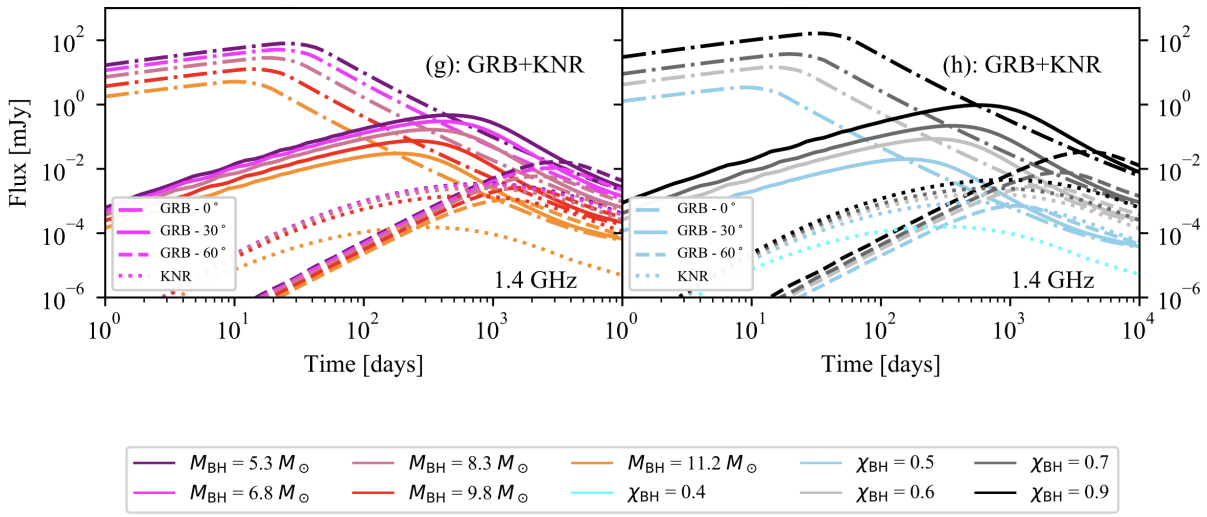

Figure 3.6: Radio light curves (1.4 GHz) from GRB afterglow emission for three viewing angles (0° dot-dashed lines, 30° filled lines, and 60° dashed lines) and the kilonova remnant (KNR, dotted lines). In the left panel for constant $\chi_{BH} = 0.8$ and varying M_{BH}. Right panel for constant $M_{BH} = 5.3\ M_\odot$ and varying χ_{BH}. With fixed parameters $M_{NS} = 1.4\ M_\odot$, $\Lambda_{NS} = 330$, luminosity distance $d_L = 230$ Mpc, constant ambient medium density $n = 10^{-3}\text{cm}^{-3}$. From Barbieri et al. [28].

The afterglow light curves show a high degree of degeneracy with respect to different combinations of binary parameters. It is not possible to infer the intrinsic parameters of the source using only the EM multi-wavelength observations alone. However, the degeneracy can be broken by performing a multi-messenger analysis with joint GW and EM signals. For example, as demonstrated in [28], by constraining the BH and NS masses from the GW signal and the redshift from the EM counterpart, information on the BH spin can be extracted from light curves. This is possible even in a very conservative setting in which the GW signal only provides information on the chirp mass, which may be the case in a GW detection with very low signal-to-noise ratio.

3.3 Detectability of afterglows

Typical jet opening angels are found in the range of $5° - 10°$ [21, 33]. Given this small angle at which the jet can be detected directly, the afterglow may be the only direct observation of the relativistic outflow from NSBH mergers. The search for the afterglow depends on whether there is a precise localization of the merger via the early isotropic kilonova signal [34]. Luckily, kilonova emission from NSBH mergers can be more luminous than from BNS mergers, as they can eject more material from the NS disruption [35]. In Figure 6 (panels a and b) of Barbieri et al. [28] the kilonova light curves from NSBH mergers for different values of BH mass and spin is shown. In all cases, the brightness of the peak flux is below ~ 23 mag.

When such a localization is possible, sensitive radio telescopes and X-ray satellites can be pointed towards this location to search for the afterglow. Sensitivity for blind afterglow searches over the GW detection area will be lower, but may still be sensitive enough to detect the afterglow [34].

We consider observers at angles much larger than the jet's core $\Theta \gg \theta_j$, where the very bright multi-wavelength emission from the relativistic jet is not detectable. The radio afterglow detectability is most robustly predicted and easiest to detect. These results can be scaled to

X-ray or optical observations [34]. Therefore, we will consider the detectability of the strongest signal at the the peak of the afterglow light curve in the radio band. We assume that most merger events will have an accurate kilonova localization, allowing for a higher sensitivity limit. As an estimation of the detectability, the current detection limit of Karl G. Jansky Very Large Array (JVLA) can be used, which is a limiting flux of $F_{\rm lim} \approx 10$ μJy at a frequency of 3 GHz [34].

Gottlieb et al. [34] have numerically determined a normalization for the analytic equation for the peak flux from Nakar et al. [36] (their Equation 10), which now takes the form

$$\begin{aligned} F_{\nu,p} = \; & 90 \left\{ \frac{g(p)}{g(2.16)} \left(\frac{\epsilon_e}{0.1}\right)^{p-1} \left(\frac{\epsilon_B}{6\times10^{-5}}\right)^{\frac{p+1}{4}} \right\} \left(\frac{E}{10^{50}\ \mathrm{erg}}\right) \left(\frac{n}{10^{-3}\ \mathrm{cm}^{-3}}\right)^{\frac{p+1}{4}} \\ & \times \left(\frac{\nu}{3\ \mathrm{GHz}}\right)^{\frac{1-p}{2}} \left(\frac{\Theta}{20^\circ}\right)^{-2p} \left(\frac{D}{40\ \mathrm{Mpc}}\right)^{-2} \mu\mathrm{Jy}. \end{aligned} \tag{3.1}$$

In this expression, E is the jet's total energy, n is the circum-merger density taken to be spacially uniform, ν is the observed frequency of the afterglow, Θ is the viewing angle and D the luminosity distance to Earth. The microphysical parameters that are least constrained are contained in the terms in the curly bracket, ϵ_e and ϵ_B, the electron and magnetic field equipartition parameters. These parameters depend only on the local conditions at the shock and describe the particle acceleration and magnetic field amplification mechanisms. p is the power-law index of the electron's distribution and the normalization numerical factor $g(p) \approx 10^{-0.31p} \left(\frac{p-2}{p-1}\right)^{p-1}$.

Equation (3.1) is normalized according to the values inferred for GW170817 but they can be adapted to other cases. It is applicable as long as the considered frequency is above the self absorption[3] and below the cooling frequency[4]. Although we focus here on the afterglow detectability in the radio band, as long as these conditions are fulfilled, the results can be applied to optical and X-ray bands as well.

In Figure 3.7, the detection horizon of an afterglow, calculated with Equation (3.1), is shown for a jet energy $E = 10^{50}$ erg and a detection in the radio band at 1.4 GHz, with a limiting flux $F_{\rm lim} = 10$ μJy. Coloured lines correspond to different circum-merger densities n. For GW170817 it was found that the merger took place in a relatively low density environment of $n \approx 10^{-3}$. Higher densities $n \gtrsim 10^{-2}$ seem to be rather common in sGRB sites [22] and enhance the detectability of an EM counterpart. For densities below the critical density $n_a \approx 10$ cm^{-3}, self absorption does not play a role and the analytic relation is valid.

We assume a power-law index of $p = 2.3$ consistent with the findings e.g. from [38], and $\epsilon_e = 0.1$, which has been shown to be typical by e.g. [39]. Since the parameter ϵ_B is less well constrained (see e.g. [40]), we choose two different values for our calculations, a low value $\epsilon_B = 10^{-4}$, and a higher value $\epsilon_B = 0.01$ used by Barbieri et al. [28].

The total jet energy of $E = 10^{50}$ erg is in good agreement with the case of $\chi_{\rm BH} = 0.6$, $M_{\rm BH} = 6\ M_\odot$, $M_{\rm NS} = 1.4\ M_\odot$ in Figure 3.6. When using the same microphysical parameters and values for n and d_L as in [28], the resulting peak flux at $\Theta = 30^\circ$ calculated with Equation (3.1) is 2.6×10^{-2} mJy. This value is close to the light gray colored curve in Figure 3.6.

[3] At low frequencies, self-absorption causes a steep cut-off of the synchrotron spectrum in a relativistic shock. The afterglow emission is well described as synchrotron emission from accelerated electrons when a relativistic shell collides with an external medium [37]. When the electron density is high enough, radiated photons propagating through the plasma scatter off synchrotron electrons, known as synchrotron self-absorption.

[4] Above the cooling frequency, cooling by synchrotron radiation is relevant and the electrons can lose a significant fraction of their energy to radiation [37].

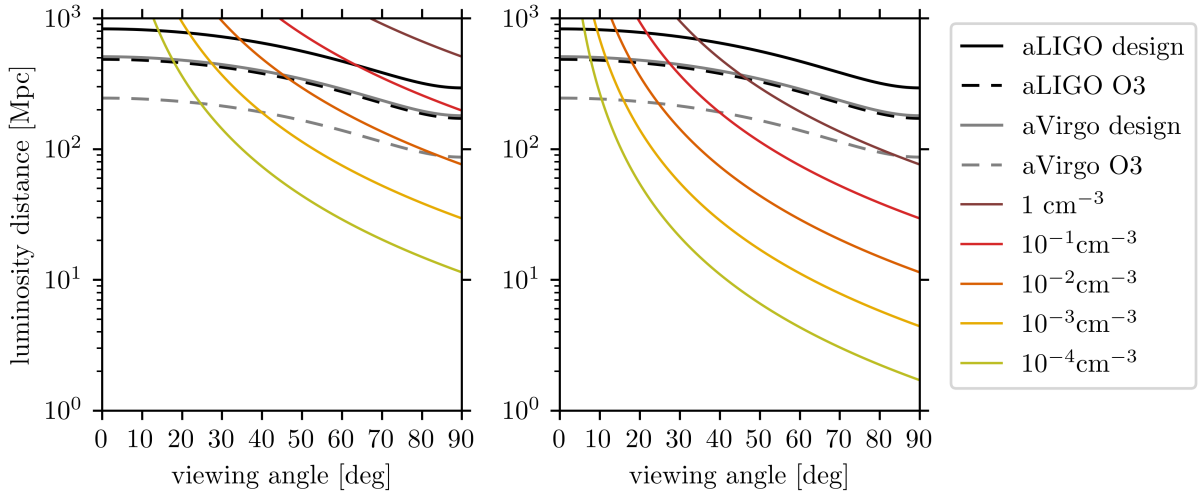

Figure 3.7: The radio (1.4 GHz) afterglow detection horizon, for a limiting flux $F_{\rm lim} = 10$ μJy and a variety of circum-merger densities (coloured lines). Also shown are the GW detection horizons of Advanced LIGO (black lines) and Virgo (gray lines) with sensitivities of observation run O3 (dashed lines) and design sensitivity (solid lines). A total jet energy of $E = 10^{50}$ erg and parameters $p = 2.3$ and $\epsilon_e = 0.1$ are assumed. In the left plot, $\epsilon_B = 0.01$ is used, in the right $\epsilon_B = 10^{-4}$. Thus, the same microphysical parameters are used on the left as in Barbieri et al. [28] and for the lightcurves in Figure 3.6.

Black and gray lines in Figure 3.7 indicate the detection horizon of gravitational-waves for Advanced LIGO and Virgo. The dependence of the GW detection horizon on the viewing angle Θ can be approximated by (from Equation 26 of Schutz [41])

$$D_{\rm GW}(\Theta) = D_0 \left[\left(1 + 6\cos^2\Theta + \cos^4\Theta\right)/8\right]^{1/2}, \tag{3.2}$$

where D_0 is the detection horizon of a face-on ($\Theta = 0$) binary system. These values for D_0 are taken from Chen et al.'s [42] online calculator, which uses the detector sensitivities indicated by [43]. We use the horizon distance, which is the farthest luminosity distance a merger could ever be detected above a signal-to-noise ratio of 8 and a binary source with masses 6 $M_\odot$ and 1.4 $M_\odot$.

For smaller viewing angles, the detection horizon of the afterglow is larger than that of gravitational-waves, and it decreases rapidly with the angle.

4 Inclination angle measurements

We will investigate inclination measurements of binary systems as obtained from EM counterparts of the merger and from gravitational-waves. In the GRB literature, the inclination angle is referred to as the viewing angle of the jet, which is the angle between the jet axis and the line of sight of the observer [44]. It is assumed that the jet is launched along the angular momentum axis of the remnant of a binary merger.

4.1 Measuring the viewing angle via an electromagnetic counterpart

We proceed by presenting the results and discussion from Nakar and Piran [20] on afterglow constraints on the viewing angle of BNS mergers. It applies also to EM bright NSBH mergers producing a relativistic jet.

A popular method to determine the geometry of an EM-bright merger is based on model fitting to the EM afterglow light curve[1]. In contrast to the kilonova light curve involving uncertainties in many aspects, the afterglow light curve is based on rather clear physics. However, the afterglow light curve alone is insufficient to determine the parameters of the geometry separately. The reason is the intrinsic degeneracy in the shape of the light curve between the jet opening angle θ_j, the viewing angle Θ and the Lorentz factor of the emitting region, Γ, as long as the jet is relativistic. Since the Lorentz factor is determined by the unknown ratio of the jet energy E and the circum-burst density n, by varying the value of this ratio, different geometries can generate similar light curves.

In what follows we want to summarize the information that different observables carry. The discussion is restricted to cases similar to GW170817, namely jets with angular structure pointing away from the observer[2], $\Theta > \theta_j$, where emission at and following the peak is dominated by the jet core and the entire afterglow curve is on the same power-law segment. The constraint $\Theta \lesssim 1$ rad ($\Theta \lesssim 60^\circ$) can be derived from the fact that the emission region is relativistic during and after the peak. Otherwise the whole light curve structure would be different.

In such jets, the light curve peaks when the relativistically beamed emission cone of the decelerating jet core spreads and starts to include the observer. Then the Lorentz factor satisfies $\Gamma \times (\Theta - \theta_j) \approx 1$ and the *peak time* t_p

$$t_p \propto \left(\frac{E}{n}\right)^{1/3} (\Theta - \theta_j) \tag{4.1}$$

E/n is expected to vary by many orders of magnitude between different mergers. So without an additional constraint on E/n, the peak time does not provide a measurement of the geometry. Also the *peak flux*[3]

[1] These light curves have been discussed in Chapter 3, especially in Figure 3.6 we have seen light curves at a frequency in the radio band.

[2] This is usually the case, because typical jet opening angles are small, as mentioned in Chapeter 3.3. Therefore, the probability that such a narrow jet is directed towards the earth is low.

[3] Symbols in this equation have already been discussed in Equation (3.1).

$$F_{\nu,p} \propto E\ n^{\frac{p+1}{4}} \epsilon_e^{\frac{p+1}{4}} \Theta^{-2p} \nu^{\frac{1-p}{2}} D^{-2} \tag{4.2}$$

depends on additional poorly constrained microphysical parameters and thus can not provide a useful constraint on the viewing angle as well.

The *rising phase of the light curve* is determined by the viewing angle as well as by the angular structure of the jet at large angles $\theta > \theta_j$. Observation of the rising phase provides only loose constraints on the jet structure. Without an a priori knowledge of the functional form of the jet structure, this phase provides no information on the system geometry.

At the peak of the light curve and the following rapid decline, the curve is dominated by the core of the jet and is similar to the one seen by an observer along the jet axis. Thus, during the *declining phase*, the light curve is independent of the viewing angle and the jet opening angle and no constraints can be obtained for either of them.

A more subtle observable is the shape of the peak, as it can be estimated only for bright enough events. The unknown detailed jet structure near the jet core, at $\theta \approx \theta_j$, governs the exact shape of the light curve close to the peak. Although this results in some freedom in modelling, the observed *peak width* provides important information. More precisely, the time between the peak and the beginning of the asymptotic decline, which is the moment when the decay becomes comparable to the one seen by an observer along the jet axis. This time difference depends on the ratio θ_j/Θ, where the peak width becomes wider with increasing value of θ_j/Θ, namely[4]

$$\frac{t_p + \Delta t_p}{t_p} \approx \left(\frac{1 + \frac{\theta_j}{\Theta}}{1 - \frac{\theta_j}{\Theta}} \right)^{1/k}, \tag{4.3}$$

where k specifies the power-law for the decay of the Lorentz factor of the emitting region, $\Gamma(t) \propto t^{-k}$. This dependence of the peak width on the ratio θ_j/Θ is shown in Figure 4.1.

A different "second order" observable is the *polarization* of the radio emission, requiring relatively strong signals for detection. Linearly polarized emission can be produced by a jet emitting synchrotron radiation. The magnitude of the polarization depends on the unknown magnetic field configuration within the emitting region. For observation at $\Theta > \theta_j$, the polarization reaches a maximum when the core of the jet becomes visible, that is around the peak time of the light curve. As discussed before, the peak time does not allow a determination of the geometry and hence polarization measurements can not be used to this aim.

It may be possible to obtain *additional constraints on the afterglow parameters* in some mergers. For example, the observed afterglow spectrum might enable an identification of characteristic break frequencies, or a constraint on the external density might be obtained by observation of the host galaxy at the location of the merger. In general, three different such additional constraints are needed to determine the geometry. The model contains six free parameters (four afterglow parameters and two for the system geometry, namely θ_j and Θ), where the light curve provides three constraints (one constraint from each of the peak time, peak flux and peak width).

We have seen that from the afterglow light curve alone, the only quantity that can be obtained on the system geometry is a constraint on the ratio of the jet opening angle and the viewing angle. Additional information is needed to break the degeneracy between the system geometry

[4]For a simple derivation of this relation, see [20].

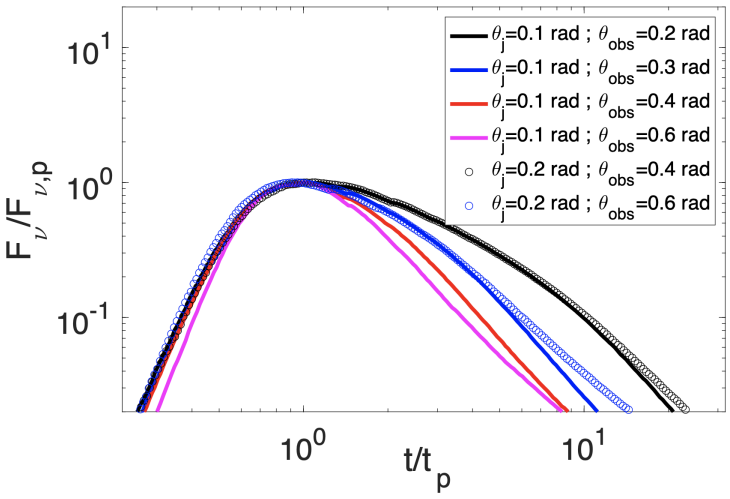

Figure 4.1: Simulated light curves from jets with different jet opening angles θ_j and viewing angles $\theta_{\rm obs}$ (named Θ in this thesis). Curves in different colours show the dependence of the peak shape on the ratio $\theta_j/\theta_{\rm obs}$, namely that the peak width becomes wider for increasing value of $\theta_j/\theta_{\rm obs}$. Two jets with different θ_j and $\theta_{\rm obs}$ but same ratio $\theta_j/\theta_{\rm obs}$ depicted in the same color (as solid line and circled line) have similar light curves as long as the emitting region is relativistic. From Nakar and Piran [20].

and afterglow parameters. This can be achieved by an independent measurement of the Lorentz factor. A useful option is measuring the superluminal motion of the centroid of the radio image with VLBI (Very Long Baseline Interferometry) observations. This enables the determination of the Lorentz factor at the time of the afterglow peak. The image of a relativistic jet seen from some angle can move at an apparent superluminal velocity $\beta_{\rm app} > 1$. The best and easiest way to measure Γ is to obtain two VLBI images around the time of the light curve peak. At this time, the apparent velocity of the image is $\beta_{\rm app} \approx \Gamma$ and the image is seen at an angle $(\Theta - \theta_j) \approx \Gamma$ with respect to the line of sight [24].

Alternatively, the degeneracy can be broken by late time observations of the light curve transition to the sub-relativistic phase. At late time, the light curves from different jets deviate from each other, because the sub-relativistic regime is reached at different times. In this regime, the beaming becomes unimportant, leading to a more moderate decay rate. These observations can reveal the earlier values of the Lorentz factor and thus allow a determination of the geometry.

Both of these methods describe "second order" observables, meaning that they require a bright afterglow with the observed peak flux being significantly higher than the detector threshold. Thus, these measurements will only be possible for relatively rare events. A critical factor necessary for a bright burst is obviously a relatively short distance, but the peak flux also depends strongly on the viewing angle. A bright afterglow requires a relatively small viewing angle. Another possible factor leading to a bright signal is a large circum-burst density.

In the case of GW170817, VLBI superluminal motion observation is the only information that can be obtained to tightly constrain Θ or θ_j. Numerous attempts to estimate these angles using the afterglow light curve alone resulted in a wide range of values. The inconsistencies of these values are largely driven by the assumed arbitrary priors of the models taken in each study. From analysis incorporating the VLBI data and including systematic uncertainties from modelling [24], the 1σ error on the viewing angle can be estimated to $\sim 15\%$.

From this discussion we have learned that a determination of the viewing angle from the elec-

tromagnetic spectrum is possible only for bright bursts. It is most effective for small viewing angles. This is convenient since the error in the viewing angle, $\delta\Theta$, is typically smaller for smaller viewing angles and is translated to an error $\delta\cos\Theta \approx \Theta\delta\Theta$. As an example, a 15% error on the viewing angle measurement of $\Theta = 10^\circ$ $(20^\circ, 30^\circ)$ translates to an error $\delta\cos\Theta \approx 0.5\%$ $(2\%, 5\%)$. Thus a very precise determination of $\cos\Theta$ can be expected at small angles. Although mergers at small angles are relatively uncommon, the enhanced emission of GWs along the system axis increases the number of observations.

4.2 Measuring the inclination with gravitational-waves

For compact binary mergers without independent redshift information from EM observations, inclination constraints from GWs remain uninformative, unless the system is close to edge-on. This follows from the distance-inclination degeneracy dominating the uncertainties for small to moderate inclinations. The obtained constraints are then mainly driven by the priors. Usually, the prior on the inclination angle is uniform on the sphere, i.e. isotropic, while the prior on the luminosity distance is uniform in volume [45]. Assuming a homogeneous isotropic population of sources in Euclidean space-time, an angle of 30° and 150° corresponds to the most likely inclination angle of GW-detected binaries [41].

Using the polarization of GW signals, the inclination angle can be determined for close to edge-on systems, for which the amplitude ratio between the two polarizations is sensitive enough to be measured [20]. But GW emission from compact binaries is not isotropic, instead more energy is emitted along the direction of the orbital angular momentum, while the least amount is emitted parallel to the orbital plane. This implies that edge-on systems need to be extremely close to be detectable [45].

Using information from an EM counterpart of a binary merger, mainly the redshift, can break the degeneracy between the inclination and the luminosity distance. Although GW detectors are able to measure the binary inclination angle ι, which also carries directional information on the rotation of the binary, most EM observations only depend on the binary viewing angle [45].

Chen et al. [45] have studied the uncertainties in viewing angle measurements. They find that if the sky positions and redshifts of BNSs can be identified via an EM counterpart and an associated host galaxy, the uncertainty in the viewing angle for 50% of the systems could be constrained to $< 7^\circ$ at 1σ. In this value, uncertainties in peculiar motion of the source and in the Hubble constant are included and account for $\sim 1^\circ$. A standard ΛCDM Planck cosmology is assumed.

The above results were obtained by simulation of 1000 detections by Advanced LIGO-Virgo at design sensitivity, with measured network signal-to-noise ratio greater than 12. The authors use an approximate Bayesian estimator assuming that sky position, chirp mass and mass ratio of the binaries are known.

To investigate how well the BNS's viewing angle can be constrained for those sources with a detectable GRB, Chen et al. [45] consider a subset of the simulated BNSs with inclination angle smaller than 25°. They find that 50% of the sources in this subsample have 1σ viewing angle uncertainty of $< 8^\circ$, if their sky locations and redshifts are known.

For NSBH systems, the errors are smaller than for BNS systems. This is because for unequal mass systems as in NSBHs there is more structure and information in the waveform as compared to equal mass systems. In the gravitational-waveform, contributions from some of the harmonics[5]

[5]In Appendix A the decomposition of the gravitational-waveform into spherical harmonics is discussed.

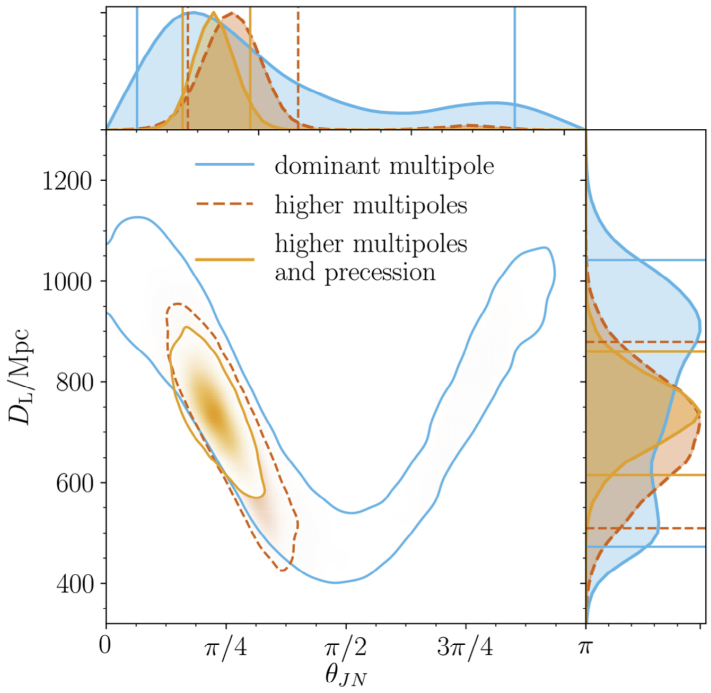

Figure 4.2: The posterior distribution of the luminosity distance D_L and the inclination θ_{JN} of GW190412. The indicated two d-dimensional area and the horizontal and vertical lines indicate the 90%credible regions. By comparing models that include either the dominant multipole, higher multipoles without precession or higher multipoles and precession, the great impact of higher multipoles on distance and inclination constraints can be seen. Higher multipoles are present in the signals from binaries with asymmetric masses. From Abbott et al.[46].

vanish for symmetric systems such as BNSs, since these contributions are proportional to the asymmetry of the system characterized by the mass ratio of the binary members. For NSBH systems, Arun et al. [44] estimate a reduction of the error in the inclination angle by $\sim 60\%$ compared to BNSs, given a 3D localiziation (sky position and redshift) from EM information.

Fixing only the sky position leads to just slightly better constraints on the inclination compared to the case where no EM information is used, for both BNS and NSBH systems. Only information from 3D localization used in the GW parameter estimation can significantly reduce the uncertainty in the inclination angle. Increasing the number of GW detectors also reduces the errors, due to the enhanced sensitivity of a network. Additionally, more detectors with distinct orientations help resolving the degeneracy between various angular parameters, which improves the inclination angle measurement [44].

Figure 4.2 illustrates the discussed distance-inclination degeneracy and the effect of unequal masses. The degeneracy between the luminosity distance and the inclination angle in the parameter estimation of GW190412 is presented. This binary black hole (BBH) system with asymmetric masses shows evidence for higher multipoles in the signal. When using models that include higher multipoles, much better constraints can be obtained for the inclination compared to when using a model that includes only the dominant multipole. If additionally the distance could be fixed, as it is possible with EM detections from NSBH mergers, even better inclination constraints can be obtained.

5 Gravitational-wave data analysis

In this chapter we will follow [47].
Detecting GW signals in detector noise requires optimized statistical methods of signal extraction. Optimal methods are well developed for situations in which the detector noise is relatively well characterized.

It is possible to construct an *optimal detection statistic*, when the statistical properties of the noise process and the exact form of the signal are known. This optimal statistic is a quantity that expresses the probability that the anticipated signal is contained in the data. Suppose that the strain data $s(t)$ recorded by a GW detector consists of a noise random process, $n(t)$ and possibly of a GW signal of known form $h(t)$. We distinguish between two hypotheses:

$$\begin{aligned} \text{Null Hypothesis} \mathcal{H}_0 : &\quad s(t) = n(t) \\ \text{Alternative Hypothesis} \mathcal{H}_1 : &\quad s(t) = n(t) + h(t). \end{aligned} \tag{5.1}$$

This is done by computing the *odds ratio* $O(\mathcal{H}_1|s) = P(\mathcal{H}_1|s)/P(\mathcal{H}_0|s)$. This is the ratio of the probability that the alternative hypothesis $\mathcal{H}_1$ is true, given the data $s(t)$, to the probability that the null hypothesis $\mathcal{H}_0$ is true given the data. To compute the odds ratio we need *Bayes' theorem*.

5.1 Bayes' theorem

First, we need to recall some definitions from probability theory. $P(\mathcal{A})$ means the probability that $\mathcal{A}$ is true, and $P(\mathcal{A}, \mathcal{B})$ is the *joint probability* that both $\mathcal{A}$ is true and $\mathcal{B}$ is true. The *conditional probability* $P(\mathcal{A}|\mathcal{B})$ is the probability that $\mathcal{A}$ is true given that $\mathcal{B}$ is true and is defined by

$$P(\mathcal{A}|\mathcal{B}) := \frac{P(\mathcal{A}, \mathcal{B})}{P(\mathcal{B})}. \tag{5.2}$$

Now we can write Bayes' theorem [48] as

$$P(\mathcal{B}|\mathcal{A}) = \frac{P(\mathcal{B})P(\mathcal{A}|\mathcal{B})}{P(\mathcal{A})}, \tag{5.3}$$

where $P(\mathcal{B})$ is called the *prior probability* of $\mathcal{B}$ being true. $P(\mathcal{A})$ is also known as the *evidence* and acts as a normalization constant. $P(\mathcal{B}|\mathcal{A})$ is the *posterior probability* of $\mathcal{B}$ being true given that $\mathcal{A}$ is true.

Bayes' theorem can be expressed in a more convenient form by using the completeness relation $P(\mathcal{A}) = P(\mathcal{A}|\mathcal{B})P(\mathcal{B}) + P(\mathcal{A}|\neg\mathcal{B})P(\neg\mathcal{B})$ where $P(\mathcal{A}|\neg\mathcal{B})$ is the probability of $\mathcal{A}$ given that $\mathcal{B}$ is not true, and $P(\neg\mathcal{B}) = 1 - P(\mathcal{B})$ is the probability that $\mathcal{B}$ is not true.

Now we can express Bayes' theorem as

$$P(\mathcal{B}|\mathcal{A}) = \frac{P(\mathcal{B})P(\mathcal{A}|\mathcal{B})}{P(\mathcal{A}|\mathcal{B})P(\mathcal{B}) + P(\mathcal{A}|\neg\mathcal{B})P(\neg\mathcal{B})} = \frac{\Lambda(\mathcal{B}|\mathcal{A})}{\Lambda(\mathcal{B}|\mathcal{A}) + P(\neg\mathcal{B})/P(\mathcal{B})}, \tag{5.4}$$

with

$$\Lambda(\mathcal{B}|\mathcal{A}) := \frac{P(\mathcal{A}|\mathcal{B})}{P(\mathcal{A}|\neg\mathcal{B})} \tag{5.5}$$

being the *likelihood ratio*. Another form of Equation (5.4) is

$$O(\mathcal{B}|\mathcal{A}) = O(\mathcal{B})\Lambda(\mathcal{B}|\mathcal{A}), \tag{5.6}$$

where $O(\mathcal{B}|\mathcal{A}) := P(\mathcal{B}|\mathcal{A})/P(\neg\mathcal{B}|\mathcal{A})$ is the odds ratio of $\mathcal{B}$ being true given $\mathcal{A}$, and $O(\mathcal{B}) = P(\mathcal{B})/P(\neg\mathcal{B})$ is the prior odds ratio of $\mathcal{B}$ being true.

5.2 Matched filter

For the problem of detection, we wish to decide between the two hypotheses in Equation (5.1); the null hypothesis $\mathcal{H}_0$ that there is no GW signal in the data, and the alternative hypothesis $\mathcal{H}_1$ that there is a GW signal contained in the data. To do so, the odds ratio for the alternative hypothesis given the observed data $O(\mathcal{H}_1|s)$ needs to be computed. With Equation (5.6) this is given by

$$O(\mathcal{H}_1|s) = O(\mathcal{H}_1)\Lambda(\mathcal{H}_1|s) \propto \Lambda(\mathcal{H}_1|s) = \frac{p(s,\mathcal{H}_1)}{p(s,\mathcal{H}_0)}, \tag{5.7}$$

where we have replaced the probabilities with probability densities. Since the prior odds ratio $O(\mathcal{H}_1)$ does not depend on the data, we are only interested in computing the likelihood ratio $\Lambda(\mathcal{H}_1|s)$.

We can compute the probability densities, if the noise is Gaussian. Recall that for a stationary Gaussian noise process $x(t)$, the probability density can be written as

$$p_x[x(t)] \propto e^{-(x,x)/2}. \tag{5.8}$$

The noise-weighted inner product (a, b) of two time-series $a(t)$ and $b(t)$ is defined as [49]

$$(a,b) := 4\ \mathrm{Re}\int_0^\infty \frac{\tilde{a}(f)\tilde{b}^*(f)}{S(f)}df, \tag{5.9}$$

where a tilde denotes the Fourier transform and an asterisk the complex conjugate. $S(f)$ is the power spectral density of the noise.

With this in mind, we can express the probability densities in Equation (5.7). Under the null hypothesis $\mathcal{H}_0$, $n(t) = s(t)$ and under the alternative hypothesis $\mathcal{H}_1$, $n(t) = s(t) - h(t)$ and so

$$\begin{aligned} p(s|\mathcal{H}_0) &= p_n[s(t)] \propto e^{-(s,s)/2}, \\ p(s|\mathcal{H}_1) &= p_n[s(t) - h(t)] \propto e^{-(s-h,s-h)/2}. \end{aligned} \tag{5.10}$$

Thus,

$$\Lambda(\mathcal{H}_1|s) = \frac{e^{-(s-h,s-h)/2}}{e^{-(s,s)/2}} = e^{(s,h)}e^{-(h,h)/2}. \tag{5.11}$$

We see that $\Lambda(\mathcal{H}_1|s)$, and thus $O(\mathcal{H}_1|s)$ depends on the data $s(t)$ only through the inner product (s,h). Since the odds ratio is a monotonically increasing function of this inner product,

$$(s,h) := 4\ \mathrm{Re}\int_0^\infty \frac{\tilde{s}(f)\tilde{h}^*(f)}{S_n(f)}df \tag{5.12}$$

is the optimal detection statistic. Any choice of threshold on the required odds ratio for accepting the alternative hypothesis can be translated to a threshold on (s,h). This inner product is called the *matched filter* [50], since it is essentially a noise-weighted correlation of the anticipated signal h with the data s.

5.3 Parameter estimation

Normally, the exact form of the signal is unknown. The possible signals are characterized by a set of parameters $\{\lambda_i\}$, which can be represented as a vector $\boldsymbol{\lambda} = [\lambda_1, ..., \lambda_N]$ in the N-dimensional parameter space of signals. We now write the gravitational-wave signal as $h(t;\boldsymbol{\lambda})$. To obtain the optimal detection statistic in this case, we must integrate out or *marginalize* over the unknown parameters. Now, the *marginalized likelihood* is

$$\Lambda(\mathcal{H}_1|s) = \int \Lambda(\mathcal{H}_{\boldsymbol{\lambda}}|s)p(\mathcal{H}_{\boldsymbol{\lambda}})d\boldsymbol{\lambda}, \tag{5.13}$$

where $\Lambda(\mathcal{H}_{\boldsymbol{\lambda}}|s)$ is the the likelihood ratio for a particular signal with parameters $\boldsymbol{\lambda}$. $\mathcal{H}_1$ is the alternative hypothesis that some signal is present and $p(\mathcal{H}_{\boldsymbol{\lambda}})$ is the prior probability distribution that describes which parameter values are intrinsically more likely.

When a strong signal with parameters $\boldsymbol{\lambda}_{\mathrm{true}}$ is present, the likelihood ratio $\Lambda(\mathcal{H}_{\boldsymbol{\lambda}}|s)$ is usually a strongly peaked function in parameter space with a value $\boldsymbol{\lambda}_{\mathrm{max}}$ at its maximum that is very close to the true parameters. When considering Gaussian noise, the logarithm of the likelihood ratio for a particular choice of parameters is

$$\ln \Lambda(\mathcal{H}_{\boldsymbol{\lambda}}|s) = (s, h(\boldsymbol{\lambda})) - \frac{1}{2}(h(\boldsymbol{\lambda}), h(\boldsymbol{\lambda})). \tag{5.14}$$

The maximum value of the likelihood ratio is achieved when

$$\left(s - h(\boldsymbol{\lambda}), \frac{\partial}{\partial\lambda_i}h(\boldsymbol{\lambda})\right)\Big|_{\boldsymbol{\lambda}=\boldsymbol{\lambda}_{\mathrm{max}}} = 0. \tag{5.15}$$

Solving this system of equations for $\boldsymbol{\lambda}_{\mathrm{max}}$, the *maximum likelihood statistic* is given by Equation (5.14) with $\boldsymbol{\lambda} = \boldsymbol{\lambda}_{\mathrm{max}}$.

For simplicity we assume that the prior probability density is a relatively constant function over the parameter ranges of interest, as it would be if we have little prior knowledge of the likely values. To estimate the true values of the parameters $\boldsymbol{\lambda}$ we can therefore focus on finding the maximum of the likelihood ratio, that is by solving Equation (5.14) for $\boldsymbol{\lambda}_{\mathrm{max}}$.

5.4 Measurement accuracy - Fisher information

We can now estimate our measurement accuracy. The detector data $s(t) = n(t) + h(t;\boldsymbol{\lambda})$ contains both noise and the gravitational-wave with the true parameter values $\boldsymbol{\lambda}$. Substituting into Equation (5.15), we find that

$$\left(h(\boldsymbol{\lambda}) - h(\boldsymbol{\lambda}_{\rm max}), \frac{\partial h}{\partial \lambda_i}(\boldsymbol{\lambda}_{\rm max})\right) = -\left(n, \frac{\partial h}{\partial \lambda_i}(\boldsymbol{\lambda}_{\rm max})\right). \tag{5.16}$$

The right hand side of these equations is a set of zero mean multivariate Gaussian random variables. We will denote them by

$$\nu^i := \left(n, \frac{\partial h}{\partial \lambda_i}(\boldsymbol{\lambda}_{\rm max})\right). \tag{5.17}$$

To calculate the measurement accuracy, we need the distribution function of $\boldsymbol{\nu}$. We will follow the derivation in [47].

The expectation value $\left\langle \nu^i \right\rangle = 0$ and the distribution of the random variables is entirely described by the *Fisher information matrix*

$$\Gamma^{ij} := \left\langle \nu^i \nu^j \right\rangle = \left\langle \left(n, \frac{\partial h}{\partial \lambda_i}(\boldsymbol{\lambda}_{\rm max})\right) \left(\frac{\partial h}{\partial \lambda_j}(\boldsymbol{\lambda}_{\rm max}), n\right) \right\rangle = \left(\frac{\partial h}{\partial \lambda_i}(\boldsymbol{\lambda}_{\rm max}), \frac{\partial h}{\partial \lambda_j}(\boldsymbol{\lambda}_{\rm max})\right), \tag{5.18}$$

where the last equality was obtained using the relation $\langle (n,g)(g,n) \rangle = (g,g)$. Therefore, the probability density function of the random variables $\boldsymbol{\nu}$ can be expressed in terms of the Fisher matrix as

$$p(\boldsymbol{\nu}) = \frac{1}{\sqrt{\det(2\pi\Gamma)}} \exp\left(-\frac{1}{2}(\Gamma^{-1})_{ij}\ \nu^i \nu^j\right), \tag{5.19}$$

with $(\Gamma^{-1})_{ij}$ being the inverse of the Fisher matrix.

Supposing that the signal is strong enough such that the maximum likelihood estimate of the parameters $\boldsymbol{\lambda}_{\rm max}$ is reasonably close to the actual value of the parameters $\boldsymbol{\lambda}$. Then the measurement error $\Delta\boldsymbol{\lambda} = \boldsymbol{\lambda}_{\rm max} - \boldsymbol{\lambda}$ is small and we can make an expansion

$$h(\boldsymbol{\lambda}) = \boldsymbol{\lambda}_{\rm max} - \Delta\lambda_i \frac{\partial h}{\partial \lambda_i}(\boldsymbol{\lambda}_{\rm max}) + \mathcal{O}\left((\Delta\boldsymbol{\lambda})^2\right). \tag{5.20}$$

Substituting this expansion into Equation (5.16) we obtain

$$\left(\frac{\partial h}{\partial \lambda_j}(\boldsymbol{\lambda}_{\rm max}), \frac{\partial h}{\partial \lambda_i}(\boldsymbol{\lambda}_{\rm max})\right) \Delta\lambda_j + \mathcal{O}\left((\Delta\boldsymbol{\lambda})^2\right) = \nu^i \tag{5.21}$$

or

$$\Gamma^{ij}\Delta\lambda_j \approx \nu^i. \tag{5.22}$$

Thus, by dropping terms of quadratic and higher order in the measurement errors we obtain the linear relationship $\Delta\boldsymbol{\lambda}_j \approx \boldsymbol{\Gamma}^{-1}\boldsymbol{\nu}$ and the distribution function for the measurement errors is

$$p(\Delta\boldsymbol{\lambda}) \approx \sqrt{\det\left(\frac{\Gamma}{2\pi}\right)}\exp\left(-\frac{1}{2}\Gamma^{ij}\ \Delta\lambda_i\Delta\lambda_j\right) \tag{5.23}$$

in the strong signal limit. This probability function shows that the inverse of the Fisher information matrix contains information about the variances of the measurement error in the parameters as well as the correlation between the measurement errors for different parameters. In particular, the root-mean-squared error in the parameter λ_i is

$$(\Delta\lambda_i)_{\rm rms} = \left\langle(\Delta\lambda_i)^2\right\rangle^{1/2} = ({\rm Var}\Delta\lambda_i)^{1/2} = \sqrt{(\Gamma^{-1})_{ii}}. \tag{5.24}$$

This Fisher information can be used to perform a systematic exploration of the $N-$dimensional parameter space of GW signals in detector noise that improves our understanding of how well we can constrain the properties of the sources of the signals.

Part II

Results

6 Estimations of κ for measurable effects of amplitude birefringence

In this chapter we consider the parametrization from Okounkova et al. [16] presented in Chapter section 2.1 to estimate the opacity parameter κ for measurable differences in the true and effective inclination. As the effective inclination ι_{eff} that is affected by amplitude birefringence, measurements from GW parameter estimation are used. For the true inclination ι, a hypothetical inclination measurement ι_{EM} from an EM counterpart is considered. The distributions for ι_{EM} and ι_{eff} are used to probe the parameter space of κ in which observable differences between EM and GW measurements of the inclination are expected. The two distributions are considered to be distinguishable when the 90% credible intervals (C.I.) no longer overlap. The hypothetical distribution of ι_{EM} is calculated such that this condition is fulfilled.

The distribution ι_{EM} is modelled as a Gaussian distribution with standard deviation of 15% or 10% of its mean value. As outlined in Chapter 4.1, a standard deviation σ of $\sim 15\%$ can be estimated for the EM measurement of the inclination angle of GW170817 from the 2σ interval reported by Mooley et al. [24]. This measurement is treated in some more detail in the coming Chapter 6.2.2. Thus, a standard deviation of $\sim 15\%$ is the accuracy seen in current inclination estimates from EM counterparts. Deeper insights into the detailed physics of an EM-bright merger and its outflows through further observations in the future and the improvement of theoretical models will reduce this uncertainty in EM inclination determinations. This is the reason for also considering a smaller standard deviation of 10%. The relative error in percent reflects the ability to measure small viewing angles with better precision via an EM counterpart than larger viewing angles.

The parameter κ is then calculated from the median values of the distributions $\iota = \iota_{\text{EM}}$ and ι_{eff} with Equation (2.7). This is the obtained lower limit of $|\kappa|$ for which an observable effect of amplitude birefringence could be seen with 90% confidence.

We apply this approach to two different GW events, namely GW190412 and GW170817. Since for the latter an EM counterpart has been observed and from that the inclination inferred, we will also use the real EM measurement to obtain a constraint on κ. Finally, we make some more general considerations.

6.1 Event GW190412: Binary black hole with asymmetric masses

The event GW190412 [46] is the first observation of an unequal-mass black hole merger. A $\sim 30\ M_\odot$ black hole merged with a $\sim 8\ M_\odot$ black hole companion. Due to the asymmetric masses, the signal contains imprints of higher multipoles. This gives more structure to the waveform and better constraints on the source properties are inferred with signal models that include higher multipoles.

The idea is to treat GW190412 as a hypothetical EM-bright NSBH merger[1]. This would correspond to an overall mass scaling.

[1]Note that just recently, the first discovery of two NSBH mergers has been published [51]. In these events, the posterior distributions of the inclination angle are bimodal and strongly correlated with luminosity distance. Thus it is not possible to obtain informative constraints from these events that could be used for our analysis.

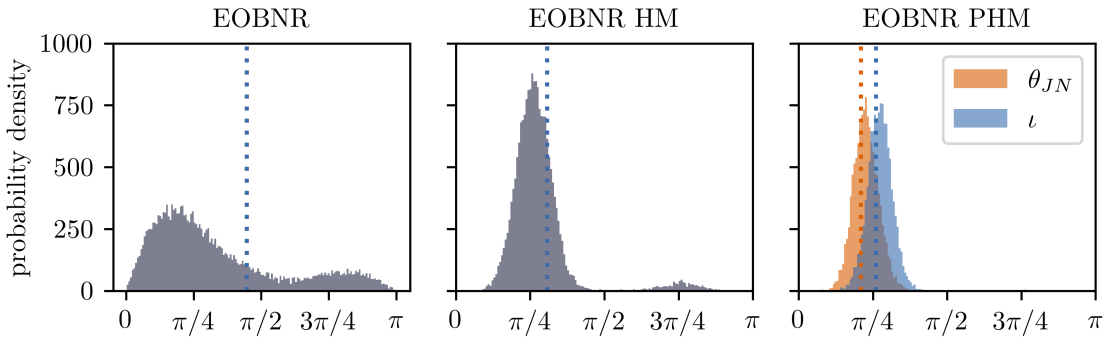

Figure 6.1: Posterior distributions of the orbital inclination ι and inclination θ_{JN} of GW190412 for the three different models described in the text. For the two models neglecting precession, the distributions are the same. Dotted lines correspond to the Maximum Likelihood value of each distribution.

The results of the GW parameter estimation [52] contain data obtained from several runs with different waveform models that were used to probe the source properties. Each of these waveform models include different amounts of physics. We will look at the inclination constraints obtained with waveform models from the EOBNR family. These models employ effective-one-body (EOB) models that are constructed from numerical relativity (NR) information completing an analytical inspiral-merger-ringdown description which builds on post-Newtonian (PN) and black-hole perturbation theory. The short names of the three models we consider are "EOBNR" (dominant multipole and no precession), "EOBNR HM" (higher multipoles and no precession) and "EOBNR PHM" (higher multipoles and precession).

6.1.1 Orbital- and total inclination angle

We want to check how well the posteriors for the total inclination θ_{JN} and the orbital inclination ι coincide for this particular event, which has marginal support for precession. Precession of the orbit occurs in binaries with spins that are not aligned with each other. For precessing binaries, $\boldsymbol{L}$ is not a stable direction but $\boldsymbol{J}$ is typically approximately constant throughout the inspiral

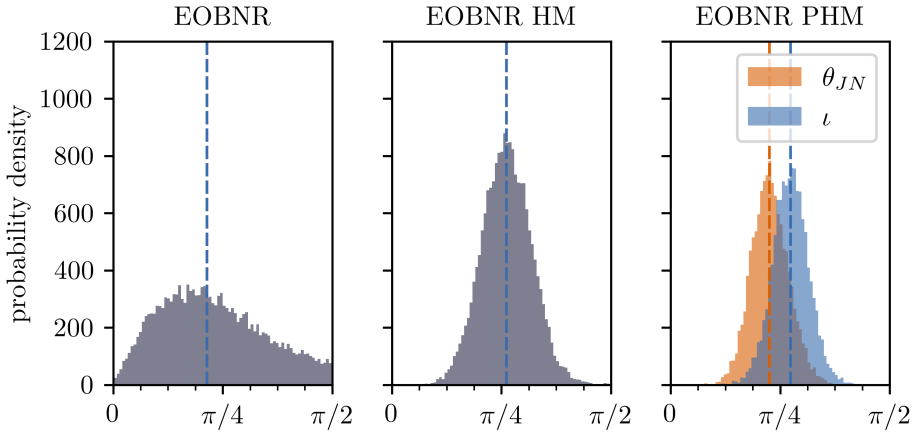

Figure 6.2: Posterior distributions of the inclination angles ι and θ_{JN} in the range [0,π/2]. Dashed lines correspond to the median value of each distribution.

[53]. In the absence of precession, θ_{JN} and ι are the same.

Figure 6.1 shows the posterior distributions of θ_{JN} and ι for the three models considered. For the third model, which includes precession, the two posteriors are slightly shifted. All three models show also some support for face-off orientations, for both angles. But clearly, a face-on orientation of the binary is favoured. So we will focus on the posterior distributions in the range [0,π/2] shown in Figure 6.2 in what follows.

The distribution for the model considering only the dominant multipole is rather uninformative. Its Maximum Likelihood value is so large that it is excluded by the other two models. The distribution peaks around the most probable angle of 30° for GW-detected binaries discussed in Chapter 4.2. Thus, this distribution is mainly driven by the priors and we will not consider it further. Instead we focus on the posteriors from the two models that include higher multipoles.

6.1.2 Modelled true and observed effective inclination

Now the distribution of the orbital inclination ι of GW190412 is used to represent the measured effective inclination angle.

The standard deviation of the Gaussian for the hypothetical true inclination angle is chosen to be 10% of its mean value. A larger σ of 15% would lead to a value of $|\kappa d_C| > 1$ for the two distributions to be separated. This is forbidden by our effective field theory treatment. Even with a standard deviation of 10%, for the model neglecting precession it is not possible to see a difference in the two distributions for values of $|\kappa d_C| < 1$. The posterior of ι_{eff} from GWs needed to be narrower, for the two distributions to be separated. For the model including precession, the posterior distribution is narrower, and a difference between the true and effective inclination can be seen for both positive and negative values of κ. These results are presented in Figure 6.3. A value of $\kappa > 1.48$ Gpc^{-1} or $\kappa < -1.51$ Gpc^{-1} would be required for a GW event like GW190412 and a joint EM inclination measurement with a 1σ uncertainty of 10% to see the effect of amplitude birefringence.

The comoving distance used in the calculations is $d_C = 0.64$ Gpc and is obtained from the median values of the luminosity distance $d_L = 0.74$ Gpc and the redshift z = 0.15 from the GW

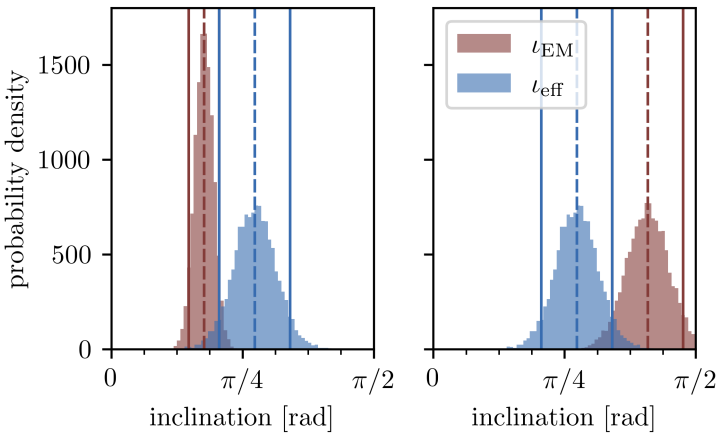

Figure 6.3: The standard deviation of the Gaussian distribution of ι_{EM} is **10**% of its mean value. The posterior distribution of the measured effective inclination ι_{eff} is presented for the model including higher modes and precession, "EOBNR PHM". Vertical lines indicate 90% credible intervals. Left: $\kappa = 1.48$ Gpc^{-1}, $\kappa d_C = 0.95$. Right: $\kappa = -1.51$ Gpc^{-1}, $\kappa d_C = -0.97$.

observation [46]. Using point values is justified under the assumption that for an event with an EM counterpart we would have much better resolved values of these quantities, e.g. from galaxy catalogues.

6.1.3 Modelled improved constraints on the effective inclination

To investigate the effect of improved constraints on the effective inclination angle from gravitational wave observations, the posterior is modelled as a Gaussian distribution with reduced width. The original width of the 90% credible interval of the posteriors for the higher-mode models, is $\sim 24°$ for "EOBNR PHM" (including precession), and $\sim 33°$ for "EOBNR HM". We now take the latter and reduce the width by 30%, 40% and 50%. Then, a Gaussian distribution centered at the median value of the original distribution with the reduced width is modelled as the effective inclination, and κ and κd_C calculated for the cases that the true and effective distributions are just separated at their 90% credible intervals. If the original width is only reduced by 20%, no separation is possible with $\kappa d_C < 1$. The obtained limits and the new widths of the 90% C.I. for ι_{eff} are summarized in Table 6.1.

An improvement in the inclination constraints from GWs is expected, when the distance to the merger can be tightly constrained by an EM counterpart. This is demonstrated by the BNS merger GW170817, where a fixed sky location and a tight distance prior from EM observations were used in the GW parameter estimation to obtain a narrow constraint on the inclination angle with a width of 22° at 90% probability[2].

A reduction in the width of ι_{eff} is also justified when considering future improvements to GW detectors or next generation detectors, where signals will be detected with higher signal to noise ratios.

If the uncertainty in the GW measurement of the inclination obtained with the waveform model "EOBNR HM" including higher modes was improved by 40% , then for $\kappa > 1.54$ Gpc^{-1} (for a 1σ error of 15% on ι_{EM}) and $\kappa > 1.32$ Gpc^{-1} or $\kappa < -1.38$ Gpc^{-1} (for a 1σ error of 10% on ι_{EM}) the GW and EM posteriors were separated by more than 90% probability for this type of event. This case is shown in Figures 6.4 and 6.5.

[2]This event will be discussed in more detail in Chapter 6.2

		standard deviation of ι_{EM}			
		15%		10%	
		effect observable for		effect observable for	
improvement	new width	κ (κd_C) >	κ (κd_C) <	κ (κd_C) >	κ (κd_C) <
30%	23°	–	–	1.47 (0.95)	−1.50 (−0.96)
40%	20°	1.54 (0.99)	–	1.32 (0.85)	−1.38 (−0.89)
50%	17°	1.40 (0.90)	–	1.17 (0.76)	−1.26 (−0.81)

Table 6.1: To examine improvements in the GW inclination constraint obtained with "EOBNR HM", the original width of the distribution is reduced by 30%, 40% and 50%. For each improvement we show the new width of the 90% C.I. of ι_{eff} and the values of κ (in units of Gpc^{-1}) and κd_C for which the two distributions ι_{eff} and ι_{EM} are just separated by their 90% credible intervals. Two different standard deviations of ι_{EM}, namely 15% and 10%, are used.

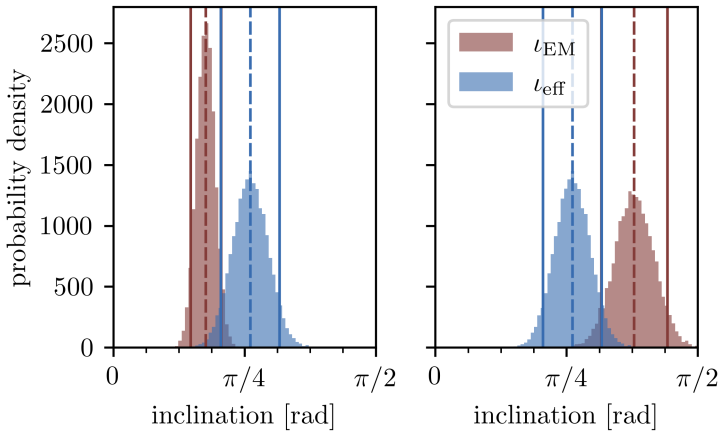

Figure 6.4: The observed effective inclination angle is modelled as a random Gaussian distribution with the same mean but width reduced by 40% compared to the posterior from parameter estimation for the model "EOBNR HM". The gaussian distribution for the true inclination has a standard deviation of **10**% of its mean value. Vertical lines indicate the 90% areas. Left: $\kappa = 1.32$ Gpc^{-1}, $\kappa d_C = 0.85$. Right: $\kappa = -1.38$ Gpc^{-1}, $\kappa d_C = -0.89$.

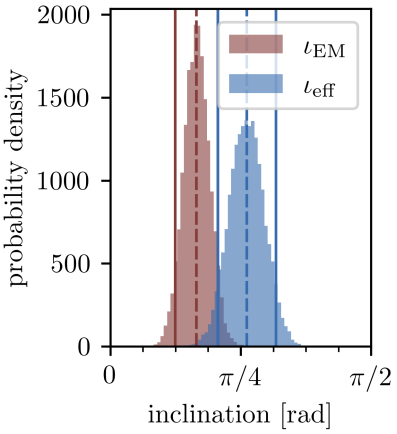

Figure 6.5: Same as in Figure 6.4 but with a standard deviation of **15**% on ι_{EM}. $\kappa = 1.54$ Gpc^{-1}, $\kappa d_C = 0.99$. For negative κ, a separation of the two distributions would require $|\kappa d_C| > 1$.

6.2 Event GW170817: Binary neutron star with observed electromagnetic counterpart

The GW detection of the first binary neutron star inspiral was made with GW170817 [54]. Additionally, tranient counterparts accross the EM spectrum have been observed. Here we investigate the inclination constraints obtained using joint GW and EM information. Observations of the EM counterpart allowed for a determination of the sky location of the merger at R.A. = 197.450374°, decl. = −23.381495° [55]. Through identification of the host galaxy NG 4993, the distance can be obtained. A precise distance measurement of 40.7 ± 2.36 Mpc was obtained based on surface brightness fluctuations of the host galaxy [56], which is independent of an assumed value of the Hubble constant H_0. Fixing the sky location in the GW parameter estimation improves the constraints on the inclination angle of the binary only little. This is in agreement with previous studies [44] exploring this correlation, as mentioned in Chapter 4.2. On

the other hand, setting a gaussian prior on the luminosity distance centered at 40.7 Mpc with a standard deviation of 2.36 Mpc results in significantly narrower posteriors on the inclination angle, and also on the source-frame chirp mass. In Figure 6.6 we show inclination posteriors obtained by [57] for three different cases; using only the GW data, fixing the sky location, and fixing the sky location and setting a gaussian distance prior. For the inclination, a prior uniform in cosι is used. This is the same prior as used in the analysis of GW190412.

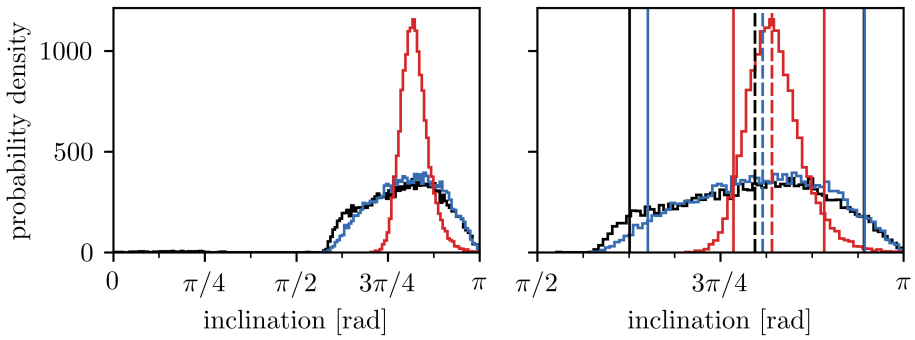

Figure 6.6: Posterior probability distributions of the inclination angle with and without combined EM information. Results for using only the GW signal are shown in black, results for fixing the sky location of the host galaxy NGC 4993 in blue, and results for both fixed sky location and a gaussian distance prior in red. On the left, the full posteriors are shown. Only the black distribution shows very little support also for angles $< \pi/2$. On the right, the same distributions but in the range $[\pi/2, \pi]$ are presented together with the 90% credible intervals (solid lines) and median values (dashed lines). Posterior data provided by Finstad et al. [57].

6.2.1 Modelled true and observed effective inclination

As previously done, we estimate the opacity parameter κ for observable differences between a hypothetical true inclination measurement from an EM observation and the effective inclination measurement from the actual GW parameter estimation with fixed sky location and a distance prior (in red in Figure 6.6). In Figure 6.7 the standard deviation of the modelled Gaussian for the true inclination $\iota_{\rm EM}$ is 10% of the mean value of the viewing angle. In that case, $\kappa > 23.7 \pm 1.4$ Gpc^{-1} or $\kappa d_C > 0.96$ would lead to observable differences. The errors in the value of κ originate from the uncertainties in d_L and z.

A standard deviation of 15% leads to $|\kappa d_C| > 1$, violating the effective field theory assumption. Also for a negative value of κ, we would need $|\kappa d_C| > 1$ for the two distributions to be separated. Although for negative κ we have $\iota_{\rm EM} > \iota_{\rm eff}$ and thus a small viewing angle for the EM inclination (the binary is face-off) with a small error (in our analysis either 10% or 15% of the mean of the viewing angle), at small true viewing angles the amplitude birefringence effect is also small (cf. Figure 2.1). Therefore a large $|\kappa d_C| > 1$ would be needed for the distributions to be separated.

For the other two cases of GW measurements, the black and blue posteriors in Figure 6.6 with broad distributions, we have $|\kappa d_C| > 1$ always.

The comoving distance $d_C = 40.3 \pm 2.3$ Mpc is obtained from EM observations of both the luminosity distance $d_L = 40.7 \pm 2.36$ Mpc [56] and redshift $z = 0.0099 \pm 0.0009$ [58].

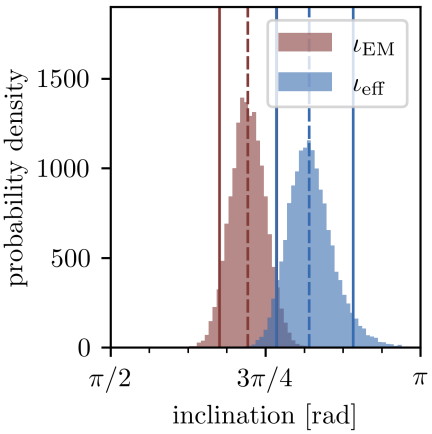

Figure 6.7: The standard deviation of the modelled Gaussian distribution of $\iota_{\rm EM}$ is **10**% of its mean value. The posterior distribution of the measured effective inclination $\iota_{\rm eff}$ is shown for the case with fixed sky location and a Gaussian prior on the distance provided by [57]. Vertical solid lines indicate 90% credible intervals, dashed lines indicate median values. A difference between the two distributions is obtained for $\kappa = 23.7 \pm 1.4$ Gpc^{-1} and $\kappa d_C = 0.96$.

6.2.2 Constraints on κ

The inclination angle of GW170817 has also been measured via the EM counterpart. By combining information from the afterglow light curve with VLBI radio imaging, the best constraints on the inclination can be obtained [21]. Mooley et al. [24] show through VLBI observations that the compact radio source exhibits superluminal motion between two epochs post merger. This measurement breaks the degeneracy between different models proposed to explain the afterglow emission, and allows for a determination of the jet opening angle and the viewing angle. General analytic considerations, largely independent of the jet structure, and a large set of numerical hydrodynamic simulations are used to find the viewing angle in the range $0.25 < \Theta < 0.50$ rad ($14^\circ - 28^\circ$), where the most likely value is $\Theta = 0.35$ rad (20°). In this range of viewing angles, all of their models consistent with the VLBI data at 2σ are included. They find that the systematic error from modelling is the dominant source of uncertainty. Therefore, this is the most accurate measurement available of the viewing angle of GW170817, since other papers that incorporated the VLBI data in their analysis considered only the statistical error of the specific models they explored[3].

In Figure 6.8 we show the GW data (for fixed sky location and distance prior [57]) together with the EM constraint (by Mooley et al. [24]) on the inclination angle. Although the EM signal can not deliver information on the orientation of the binary (i.e. face-on or face-off), the GW data clearly indicates a face-off orientation. Thus the inclination angle can be computed via $\iota_{\rm EM} = \pi - \Theta$, and so at 2σ we have $2.64 < \iota_{\rm EM} < 2.89$ rad ($151.4^\circ - 165.7^\circ$), with the most probable value at 2.79 rad (159.9°). The GW data indicates $\iota_{\rm GW} = 147.9^{+12.4}_{-9.6}$ degrees at 90% confidence [57].

These two inclination measurements can be used to place bounds on κ and constrain amplitude birefringence. With Equation (2.7) and $\iota = \iota_{\rm EM}$ as true incination and $\iota_{\rm eff} = \iota_{\rm GW}$ as the effective inclination potentially subject to amplitude birefringence, κ can be calculated. To place an upper bound on κ, the lowest value from the EM range $\iota = \iota_{\rm EM} = 2.64$ rad, and the largest

[3] see [20] for a detailed discussion.

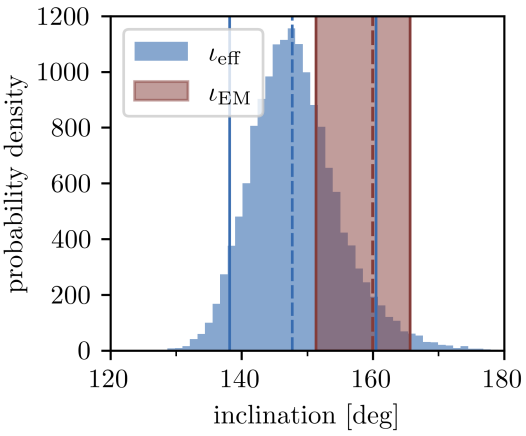

Figure 6.8: Inclination constraints for GW170817 from GW parameter estimation [57] (denoted as $\iota_{\rm eff}$ with median (dashed line) and 90% credible interval) and from EM observations [24] (with the most probable value (dashed line) and 2σ range indicated by vertical lines). From these measurements, an upper bound $\kappa < 20.2$ Gpc^{-1} can be obtained.

value from the GW 90% credible interval $\iota_{\rm eff} = \iota_{\rm GW} = 160.3° = 2.798$ rad is taken. With the luminosity distance 40.7±2.36 Mpc (the error corresponds to the quadrature sum of statistical and systematic errors reported in [56]) and redshift $z = 0.0099 \pm 0.0009$ [58], κ is calculated to $\kappa = 19.1 \pm 1.1$ Gpc^{-1}, when taking into account the errors on d_L and z. Thus, we can place an upper bound $\kappa < 20.2$ Gpc^{-1}, where $\kappa d_C < 0.77$.

A lower bound on κ can not be obtained within the effective field theory regime $|\kappa d_C| < 1$. The very close distance of GW170817 makes it difficult to probe amplitude birefringence and place tight bounds on κ. Better constraints will be obtained for EM bright binary sources farther away.

However, the large difference between the most probable inclination values from both measurements is remarkable. When using these most probable values $\iota_{\rm EM} = 2.79$ rad and $\iota_{\rm eff} = 147.9° = 2.58$ rad, we obtain a value $\kappa = -24.2$ Gpc^{-1} and $\kappa d_C = -0.97$, which would be a huge effect. But since the two distributions still overlap largely, $\kappa = 0$ can not be ruled out.

The event GW170817 with its GW and EM measurements of the inclination favours rather negative values of κ. If $\kappa < 0$, the effective inclination in GW parameter estimation would be smaller than the true inclination. This birefringence effect would be larger for face-off systems. Thus, constraining κ or actually seeing an effect would best be possible with face-off systems, if $\kappa < 0$.

6.3 More general considerations

We have looked at specific GW events so far, with given distance and median values of the inclination. To investigate how estimations of κ for a measurable difference between the true and effective inclination depends on the distance and median value of the true inclination, we will look at this parameter space in the contour plots in Figure 6.9. We fix the width of both distributions and determine the value of κ, such that the two distributions are just separated. The width of the distribution for $\iota_{\rm eff}$ is fixed to the width of the 90% credible interval of GW170817 (the posterior with fixed sky location and distance prior), namely to $\Delta\iota_{\rm eff} = 22.0°$ [57]. For a Gaussian distribution of $\iota_{\rm EM}$ we estimate the width of the 90% credible interval as

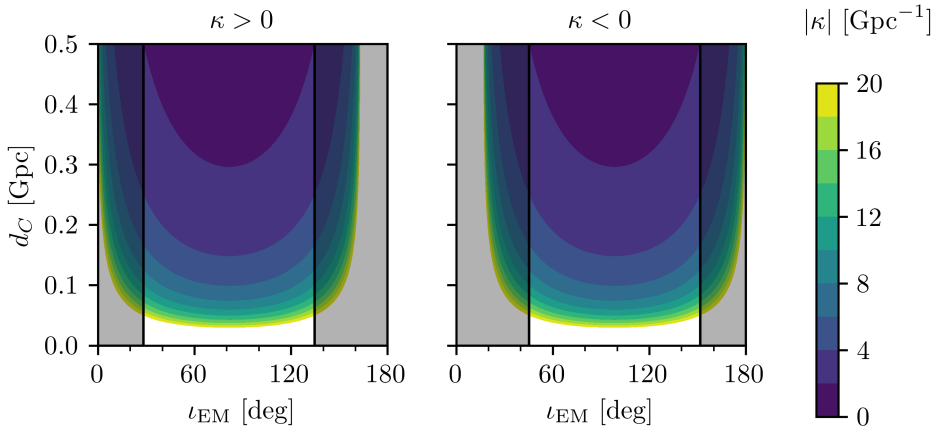

Figure 6.9: Contour plot for $|\kappa|$ depending on the comoving distance d_C and the true inclination $\iota_{\rm EM}$ for fixed widths of the distributions of $\iota_{\rm eff}$ and $\iota_{\rm EM}$.

$\Delta\iota_{\rm EM} = 0.206$ rad (11.8°) from the 2σ range reported by Mooley et al. [24] for GW170817 discussed above. $\Delta\iota_{\rm EM} = 0.206$ rad (11.8°). We assume symmetric distributions and calculate κ with Equation (2.7) and ι and $\iota_{\rm eff}$ being the values in the center of the range $\Delta\iota_{\rm eff}$ and $\Delta\iota_{\rm EM}$ respectively.

Note that here we fix the width of $\iota_{\rm EM}$ for all angles and do not take into account that measuring the inclination angle electromagnetically for close to edge on mergers is impossible[4]. Also not taken into account here is that the accuracy of the GW measurement would decrease with large distances when the amplitude of the signal decreases.

Still we can see the expected trends, namely that κ is smaller for larger distances or/and larger viewing angles. At small viewing angles, $\kappa d_C > 1$ would be needed for the two distributions to be separated. The smallest viewing angles $\Theta \gtrsim 28.4°$ are allowed for face-on systems when $\kappa > 0$ and for face-off systems when $\kappa < 0$.

To make an example, we pick a luminosity distance of 300 Mpc and redshift 0.07, resulting in a comoving distance $d_C = 0.28$ Gpc. For a median true inclination at $\iota_{\rm EM} = 30°$ and $\kappa > 0$, or $\iota_{\rm EM} = 150°$ and $\kappa < 0$, the amplitude birefringence effect is seen for $|\kappa| > 3.43$ Gpc^{-1} and $|\kappa d_C| > 0.96$.

Using instead a comoving distance $d_C = 0.37$ Gpc corresponding to $d_L = 400$ Mpc and $z = 0.09$, we obtain $|\kappa| > 2.62$ Gpc^{-1} and $|\kappa d_C| > 0.96$.

For both distances, when $\iota_{\rm EM} = 30°$ and $\kappa < 0$, or $\iota_{\rm EM} = 150°$ and $\kappa > 0$, we can not apply the formalism since $|\kappa d_C| > 1$.

To generalize further, we consider a wide range of widths of the effective inclination distribution $\Delta\iota_{\rm eff}$ as a function of κd_C in Figure 6.10. This is the maximum width for which the two distributions $\iota_{\rm eff}$ and $\iota_{\rm EM}$ are separated, where the width $\Delta\iota_{\rm EM}$ is the 90% C.I. The colours of the plotted curves correspond to different mean values of the viewing angle of $\iota_{\rm EM}$. These distributions for $\iota_{\rm EM}$ are Gaussian with either a standard deviation of 10% (solid lines) or 15% (dashed lines) of the viewing angle of their mean values.

[4]In Chapter 4.1 we discussed that only for $\Theta \lesssim 60°$ it is possible to observe an afterglow light curve with a peak that carries information about the viewing angle.

These plots show again the fact that the amplitude birefringence effect is larger for face-on systems when $\kappa > 0$ and for face-off systems when $\kappa < 0$.

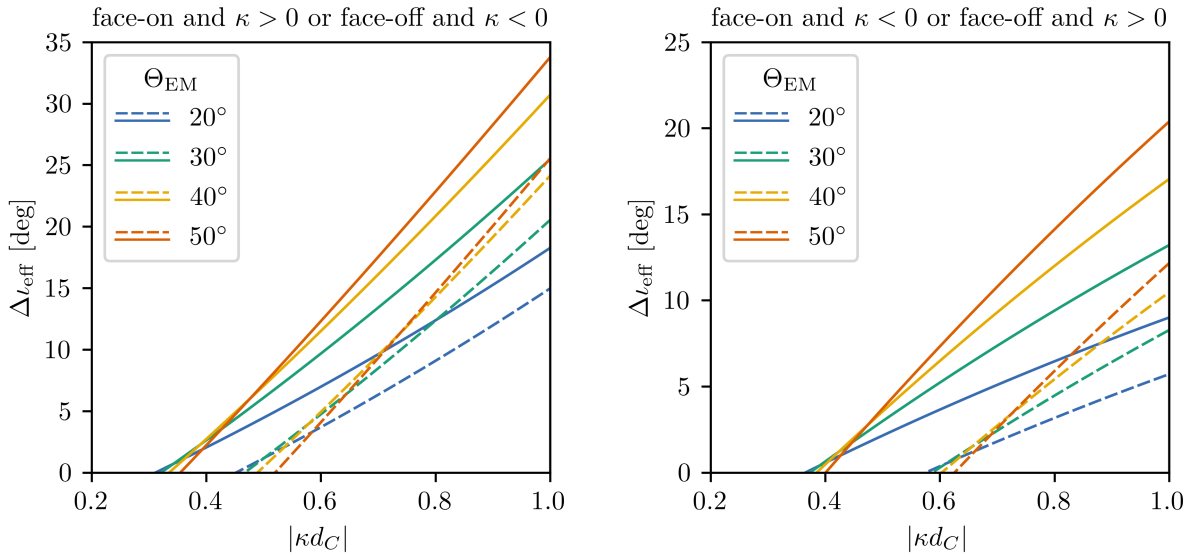

Figure 6.10: Width of the posterior distribution of the effective inclination angle ι_{eff} as a function of $|\kappa d_C|$ for different values of the true viewing angle Θ_{EM}. For face-on systems, the inclination angle is identical to the viewing angle and for face-off systems, $\iota_{\mathrm{EM}} = 180° - \Theta_{\mathrm{EM}}$. Solid and dashed lines correspond to a standard deviation for Θ_{EM} of 10% and 15% respectively.

7 Parameter estimation via Fisher information

To study more systematically how well one can constrain amplitude birefringence, we perform a Fisher information analysis, as it is described in Chapter 5.4. For this aim we adapt a private Mathematica code written by Chandra K. Mishra. This code was used by LIGO for the BNS event GW170817 to test for waveform deviations from general relativity using a parametrized waveform expansion and to place bounds on non-GR parameters. These are two-detector bounds with the PSDs[1] taken around GW170817 for each of the Advanced LIGO detectors (Livingston and Hanford). The waveform is constructed with the source parameters from the GR production parameter estimation runs. For each parameter we randomly select 1000 posterior samples. We introduce a parameter for amplitude birefringence to the waveform and with the Fisher information matrix calculate the expected 1σ deviation of this parameter from zero.

7.1 Expected trends

Using the formalism of Okounkova et al. [16] discussed in Chapter 2, we introduce an effective inclination angle that depends on the true inclination angle and κd_C. The original code is working with a simplified Fourier domain waveform that does only depend on the intrinsic parameters and the distance. To consider the dependency on the inclination angle, we compute the plus and cross polarizations to obtain the new frequency-domain waveform $h(f) = h_+ - ih_\times$. Using the inclination dependency of the dominant modes given in Equation (A.7) we can write

$$h_+ = \frac{1}{2}(1+\cos^2\iota)\mathcal{A}e^{i\Psi}, \qquad h_\times = i\cos\iota\mathcal{A}e^{i\Psi}. \tag{7.1}$$

Then, the complex strain can be obtained as

$$h(f) = h_+ - ih_\times = \mathcal{A}e^{i\Psi}\left[\frac{1}{2}(1+\cos^2\iota)+\cos\iota\right]. \tag{7.2}$$

By multiplying the waveform[2] in the original code with this inclination dependent factor in the square brackets, we reintroduce the inclination dependence that has been averaged over for the original purpose of the code. By setting $\iota = \iota_{\text{eff}}$ given in Equation (2.8) we obtain the dependency of the strain on the true inclination and the birefringence parameter κd_C.

Initially, κd_C is set to zero and its deviation from zero $\Delta(\kappa d_C)$ is obtained via Fisher information. We model the true inclination as a Gaussian distribution with mean value 159.9° and standard deviation 7.2°, which corresponds to the EM measurement [24] of GW170817 discussed in Chapter 6.2.2. The 1σ error in our estimation of κd_C for this system as obtained from the inverse of the Fisher matrix is shown in Figure 7.1. By taking the median value over all 1000 samples, we obtain an estimate of $\kappa d_C = 0 \pm 0.011$. Using the comoving distance to GW170817, $d_C = 40.3 \pm 2.3$ Mpc discussed in Chapter 6.2.1, we obtain a constraint on the error in the

[1] The PSDs have been fitted and are part of the private code.

[2] The original waveform is unimportant for our purposes. Our Fisher analysis of amplitude birefringence depends only on our newly introduced factor.

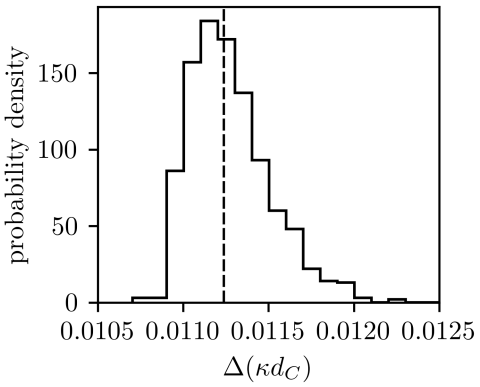

Figure 7.1: The distribution of $\Delta(\kappa d_C)$ as obtained from Fisher information. For the source parameters, the original posterior distributions from GW170817 are used.

opacity parameter $\Delta\kappa = 0.27 \pm 0.02$ Gpc^{-1} that would translate to an upper bound $|\kappa| < 0.29$ Gpc^{-1}.

We investigate possible trends in $\Delta(\kappa d_C)$ when varying the extrinsic parameters of the binary. In particular, we use different values for the mean μ and standard deviation σ of the Gaussian distributions for the true inclination and the signal-to-noise ratio (SNR). The resulting distributions in $\Delta(\kappa d_C)$ when changing the SNR and keeping the other parameters fixed are shown in Figure 7.2 and when changing the true inclination while fixing the other parameters is shown in Figure 7.3. The 1σ uncertainty in our Fisher estimation of $\Delta(\kappa d_C)$ for all these cases is presented in Table 7.1.

As expected, $\Delta(\kappa d_C)$ decreases with increasing SNR. In Fisher information, the measurement error is proportional to 1/SNR, which is confirmed by our data. The uncertainty in the SNR, i.e. the width of the distribution, has no effect on the median value of $\Delta(\kappa d_C)$ but only on the

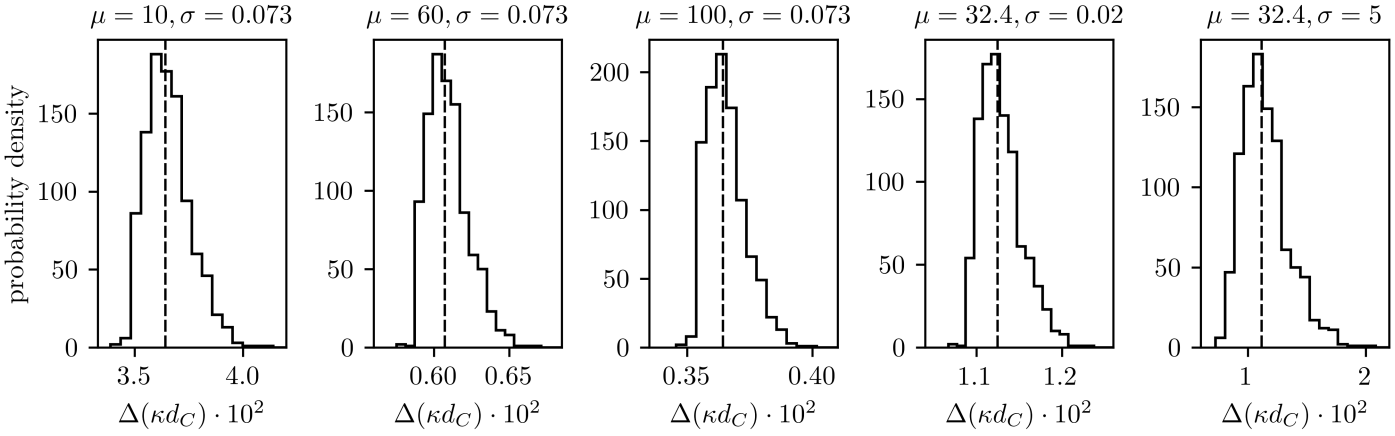

Figure 7.2: Changing the SNR in the Fisher analysis of the error in κd_C, that is its deviation from zero, $\Delta(\kappa d_C)$. In the title of each subplot we show the mean μ and standard deviation σ of the modelled Gaussian distribution for the SNR. The other parameters are fixed to the posterior distributions from GW10817, whereas the original SNR has a median of 32.424 and standard deviation 0.073. Dashed lines indicate the median values of $\Delta(\kappa d_C)$ over all 1000 samples.

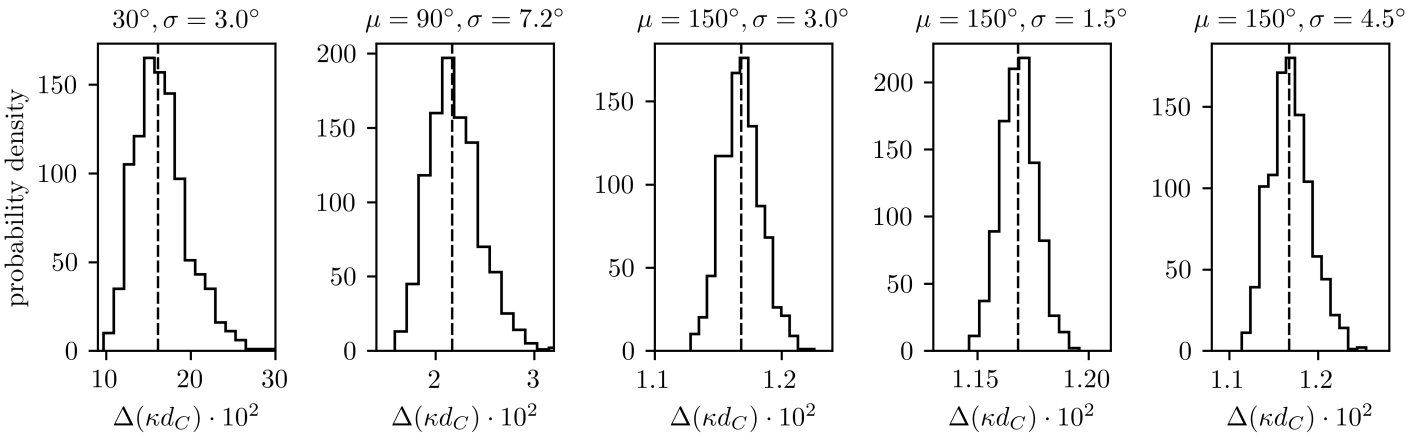

Figure 7.3: Same as in Figure 7.2 but for changing the true inclination instead of the SNR. The original true inclination inferred from the EM counterpart of GW170817 is modelled as a Gaussian distribution with mean and standard deviation $159.9° \pm 7.2°$.

spread of the individual samples.

When changing the true inclination we observe a decrease in $\Delta(\kappa d_C)$ with inclination. This behaviour has not yet been fully understood at the time of writing. According to Equation (7.2) the amplitude decreases with inclination. We expect this reduced signal to translate to a decrease in effective SNR, which should lead to a decrease in mesurability of $\Delta(\kappa d_C)$. From these considerations we expect that an increasing true inclination, and thus increasing ι_{eff}, would result in larger errors $\Delta(\kappa d_C)$. This is the opposite behaviour of what is seen in our results from the code.

As in the previous case, the width of the distribution of the true inclination does not change the median value of $\Delta(\kappa d_C)$ but is directly related to the spread of the individual samples only.

SNR	inclination	$\Delta\kappa d_C$
32.424 ± 0.073	159.9°± 7.2°	0.011
10 ± 0.073	159.9°± 7.2°	0.036
60 ± 0.073	159.9°± 7.2°	0.0061
100 ± 0.073	159.9°± 7.2°	0.0036
32.4 ± 0.02	159.9°± 7.2°	0.011
32.4 ± 5	159.9°± 7.2°	0.011
32.424 ± 0.073	30°± 3°	0.16
32.424 ± 0.073	90°± 7.2	0.022
32.424 ± 0.073	150°± 3°	0.012
32.424 ± 0.073	150°± 1.5°	0.012
32.424 ± 0.073	150°± 4.5°	0.012

Table 7.1: Results from Fisher analysis of the estimated deviation of the amplitude birefringence parameter from zero, $\Delta(\kappa d_C)$. The original distributions of the SNR and true inclination for GW170817 are shown in the first line as mean ± standard deviation. By varying each of these distributions separately, we observe the resulting trends in $\Delta(\kappa d_C)$.

Since our Fisher parameter κd_C appears in a frequency independent scale factor on the overall amplitude of the waveform, we have that $\Delta(\kappa d_C)$ varies only when changing the true inclination or the SNR. Therefore, using Fisher information, the error in the birefringence parameter $\Delta(\kappa d_C)$ is independent of the exact form of the waveform but only depends on our introduced amplitude factor and the SNR. This is because Fisher information captures only first order effects in the high SNR limit [59]. To see an effect from more subtle features like improved constraints on the observed inclination from asymmetric masses, as well as from independent EM distance constraints and improved independent constraints on the true inclination angle (from a hypothetical EM counterpart), a beyond Fisher formalism or full Bayesian parameter estimation would be required.

7.2 Frequency dependent amplitude birefringence

Using the formalism for amplitude birefringence described in Chapter 1.2 that maintains the original frequency dependence of the correction terms, we can write

$$h_R = h_R^{\mathrm{GR}}\, e^{\pi f \tilde{\kappa}}, \qquad h_L = h_L^{\mathrm{GR}}\, e^{-\pi f \tilde{\kappa}}. \tag{7.3}$$

Now we obtain the complex strain with the relations for h_+ and $h_\times$ given in Equation (1.9) as

$$h_+ - i h_\times = (h_+^{\mathrm{GR}} - i h_\times^{\mathrm{GR}})\, e^{\pi f \tilde{\kappa}}. \tag{7.4}$$

Therefore, we can multiply the original waveform in the Fisher code with the factor $e^{\pi f \tilde{\kappa}}$ to obtain the parity violating waveform with parametrized deviations from GR encoded in $\tilde{\kappa}$. Now the estimated error in $\tilde{\kappa}$, i.e. its 1σ deviation from zero $\Delta\tilde{\kappa}$, is sensitive to changes in the frequency dependency of the waveform amplitude (the original amplitude of the GR waveform is proportional to $f^{-7/6}$) in addition to changes in the PSD or the SNR. The resulting distribution of $\Delta\tilde{\kappa}$ from 1000 samples using the original parameters for the SNR and PSD from GW170817 is shown in Figure 7.4. The distribution of $\Delta\tilde{\kappa}$ with median and standard deviation is obtained as $\Delta\tilde{\kappa} = 4.239 \pm 0.009 \times 10^{-5}$ seconds. This allows us to estimate an upper bound $|\tilde{\kappa}| < 4.2 \times 10^{-5}$ seconds.

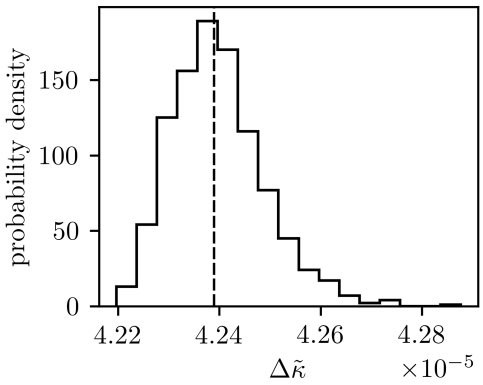

Figure 7.4: The distribution of $\Delta\tilde{\kappa}$ obtained from Fisher information with parameter values from GW170817.

With this constraint on $\tilde{\kappa}$ we can calculate an upper bound on the Chern-Simons length scale l_0 for a canonical field profile via Equation (1.30). We adopt a Planck cosmology with present day Hubble constant $H_0 = 67.8$ km/s/Mpc [60] and use the comoving distance to GW170817, $d_C = 40.3 \pm 2.3$ Mpc discussed in Chapter 6.2.1. Using these values we estimate an upper bound on the Chern-Simons length scale $l_0 < 4.9 \times 10^2$ km. A thorough discussion of existing bounds on amplitude birefringence and their mapping on to a Chern-Simons length scale can be found in [5].

Since our Fisher information on $\Delta\tilde{\kappa}$ does not depend on the phase of the waveform, but only on our $\tilde{\kappa}$-dependent amplitude factor, we can explore constraints on l_0 with different comoving distances to the source and different SNRs. In Figure 7.5 we show the upper bound on the Chern-Simons length scale l_0 as a function of the comoving distance for different values of the SNR. The trend is clear; l_0 can be better constrained for increasing SNR and/or increasing distance. To conclude, Fisher information suggests that tighter bounds on l_0 can be placed for louder and further events, where the quantitative dependence on SNR and d_C is shown in Figure 7.5.

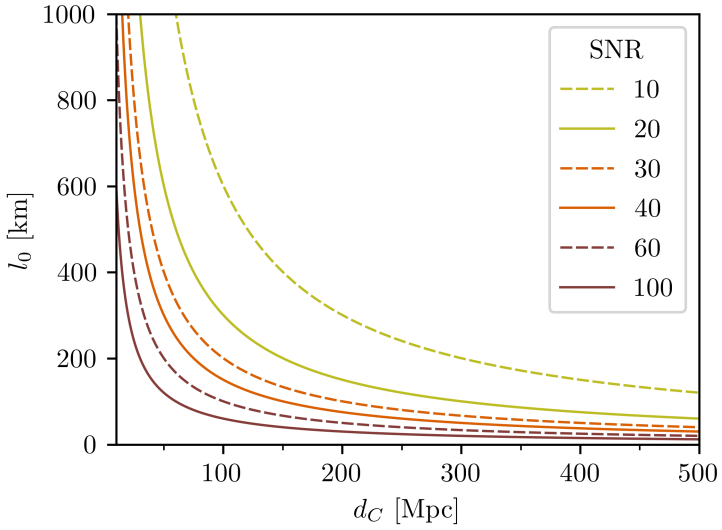

Figure 7.5: Upper bound on the Chern-Simons length scale l_0 for the canonical CS field profile as a function of the comoving distance, for different values of the signal-to-noise ratio (SNR).

Conclusion

Gravitational parity violation changes the amplitude and phase of the circular polarizations of gravitational-waves, which is called amplitude and velocity birefringence respectively. In parity-violating gravity theories that predict amplitude birefringence, such as Chern-Simons gravity, the amplitudes of the right- and the left-circularly polarized GW modes are either enhanced or suppressed during propagation. This amplitude correction is degenerate with the inclination angle, the distance and location of the source in the sky [4]. Amplitude birefringence leads to an apparent change in the inclination of a binary system as observed by GW detectors, which is strongest at large viewing angles. The inclination of a binary as measured with GWs can be better constrained when the binary component masses are asymmetric or when the distance and sky location is obtained from an independent electromagnetic measurement. This makes EM-bright neutron star-black hole binary mergers interesting sources for studying amplitude birefringence, because the correction is not degenerate with other parameters in the model [10].

If an EM counterpart is produced in a NSBH merger, its distance, sky location, and possibly its inclination can be inferred electromagnetically. In a subsequent GW parameter estimation, these parameters can be fixed or appropriate priors specified. Using waveform templates that include a parameter that characterizes the strength of birefringence it is possible in principle to place constraints on parity violation.

Another source for multi-messenger observations of compact binary mergers are binary neutron stars. Gravitational-waves, a coincident short gamma-ray burst and other transient counterparts across the EM spectrum have been observed for GW170817, the first detection of GWs from a BNS. These EM counterparts allowed for a determination of the sky location, and the distance to the source was obtained through identification of the host galaxy. Furthermore, an EM determination of the inclination angle has been achieved.

An EM counterpart is only produced in NSBH mergers, if the neutron star is tidally disrupted and an accretion disc is formed around the remnant black hole. Such a tidal disruption taking place outside of the innermost stable circular orbit of the BH is expected for highly spinning, low mass BHs. An examination of the parameter space suggests that BHs with masses around $\sim 6\ M_\odot$ and dimensionless spins around ~ 0.6 would be required.

After the merger of both types of systems, NSBHs and BNSs, mass accretion onto the remnant BH can power the launch of a relativistic jet along the angular momentum axis of the remnant, potentially leading to the production of a short GRB. Long lasting X-ray, optical and radio afterglow emission is produced during the interaction of the relativistic jet with the interstellar medium. Observation of the afterglow light curve (i.e. the flux observed with time at a specific frequency) can allow for a measurement of the inclination angle of the binary system. In most cases, the jet is directed away from us at a certain viewing angle. The larger the viewing angle and distance to the binary merger, the fainter is the observed afterglow.

If one aims for an EM determination of the viewing angle of BNSs or NSBH binaries, the viewing angle and distance should not be too large, otherwise the afterglow would not be detectable. On the other hand, the apparent change in the inclination angle encoded in GWs caused by the birefringence of polarizations is larger at larger viewing anlges. Therefore, a binary at a moderate viewing angle of $\sim 30^\circ$ seems ideal for testing GW amplitude birefringence via EM and GW inclination constraints.

Adapting a formalism from [16] we try to constrain a parameter κd_C that measures the relative suppression/enhancement between the right-handed and left-handed polarizations of the GW as an effect of parity violations on the observed inclination angle, where d_C is the comoving distance to the source. We estimate how large the birefringence effect, characterized by κd_C, would need to be in order to observe a measurable difference in the effective and the true inclination. The true inclination constraints are assumed from a hypothetical EM counterpart whereas the effective inclination constraints are obtained from GW parameter estimation results of two different events, namely GW190412 with asymmetric BH masses and the BNS merger GW170817 with actual independent EM distance and inclination constraints. We treat GW190412 as a hypothetical NSBH merger with an overall mass scaling. The mass ratio of the black holes in GW190412 is similar to that of EM-bright NSBH mergers. This asymmetry allows for a reasonably well constrained inclination measurement from the GW observation, due to the presence of higher order multipole moments in the signal. Note that we do not consider the two NSBH coalescences, whose detection has just recently been published [51], because their inclination posteriors are bimodal and strongly correlated with the luminosity distance. Thus they do not provide informative constraints that can be used in our analysis.

For both systems, we estimate that $|\kappa d_C| > 0.95$ would be required to have the effective and true inclination distributions separated at their 90% credible intervals. Even from investigations of improved constraints on the GW measurement of the effective inclination we find that for a directly observable effect $|\kappa d_C| > 0.76$ is needed in the case where the width of the 90% C.I. is reduced by 50%. Still it is possible to place an upper bound on $|\kappa d_C|$ from the actual GW and EM measurements of the inclination of GW170817, that is $\kappa d_C < 0.77$. Using the comoving distance $d_c = 40.3 \pm 2.3$ Mpc as obtained from EM observations, we obtain an upper bound $\kappa < 20.2$ Gpc^{-1}.

We then pursue a Fisher analysis that enables us to make more general statements on the mesurability of birefringent effects and that is not restricted to available GW data. This allows us to probe also the dependence on the signal-to-noise ratio. Fisher information can be used to estimate the measurement errors on parameters of GW signals in detector noise and improves our understanding of how well we can constrain the source properties of signals. Via Fisher information we estimate the measurement error in κd_C, namely its 1σ deviation from zero. Using the posterior distribution from parameter estimation of the SNR of GW170817 and the true inclination as obtained from the EM counterpart, we estimate a measurement error $\Delta\kappa d_C = 0.011$. This expected error around zero is much smaller than the values at which a separation of the effective and true inclination could be observed at 90% confidence. From this we conclude that even in the case of well constrained inclinations from GWs, with independent EM observations of the distance and sky location and in unequal mass binaries, it would not be possible to see the effect of birefringence through distinguishable measurements of the effective and true inclination.

An inaccuracy of the order of $\Delta\kappa d_C < 0.011$ (in an underlying assumption of non-existent birefringence effects) would translate to an error in the Hubble constant as measured via GWs of less than $\sim 1\%$. This means that, particularly for the Hubble constant measurement with GW170817, such an inaccuracy would not have affected the measurement of the Hubble constant considerably.

We also use Fisher information in a frequency dependent, an thus more general formalism of amplitude birefringence. This time, we introduce the birefringence effect characterized by $\tilde{\kappa}$ not via an apparent inclination angle to a GR waveform, but by directly implementing the parity violated left- and right-polarized modes. Since the amplitude correction factor to the waveform

is frequency dependent and so is its derivative with respect to $\tilde{\kappa}$, we have that the Fisher Matrix element that gives the estimated error $\Delta\tilde{\kappa}$ now depends on the noise power spectral density of the detectors, in addition to the signal-to-noise ratio. When taking the PSDs of the two LIGO detectors around the time of GW170817 and the posterior distribution of the SNR for that event, an error estimate of $\Delta\tilde{\kappa} = 4.2 \times 10^{-5}$ seconds is obtained. Using this as a constraint on $\tilde{\kappa}$, we estimate an upper bound on the Chern-Simons lenght scale for a canonical CS field profile, that is $l_0 < 4.9 \times 10^2$ km, where the comoving distance to the binary is assumed to correspond to the one obtained for GW170817. Since the estimated parameter errors in Fisher information are proportional to 1/SNR, we can scale our bound to different SNRs and use different distances in our calculation of l_0 from $\tilde{\kappa}$. We then obtain Fisher estimations of an upper bound on the Chern-Simons length scale depending on the SNR and distance.

Outlook

Fisher information captures first order effects in the high SNR limit. We could wish for more realistic estimates of bounds that can be placed on amplitude birefringence that depend on the binary parameters such as the masses, mass ratio and distance, and in particular on how well each parameter can be constrained. This could be obtained from a simulated parameter estimation, with assumed EM distance prior and fixed sky location.

If an independent inclination constraint from an EM counterpart is assumed, one could implement an effective inclination depending on $\tilde{\kappa}$ and the true inclination in a GR gravitational-wave template to model the birefringence effect. These templates can be used for injections of fake GW signals into real or simulated noise. The simulated GW data can then be interpreted via GR source parameter estimation, i.e. with a template model that does not include $\tilde{\kappa}$, to study the recovery of the observed inclination angle depending on $\tilde{\kappa}$.

Alternatively, one could use a parity violating waveform template from the expressions for the plus and cross polarizations that depend on $\tilde{\kappa}$ to study the recovery of $\tilde{\kappa}$ from the fake GW data for different injected values of $\tilde{\kappa}$.

This analysis could be applied to the actual GW data from GW170817. Estimating the parameters with a fixed sky location and a distance prior as obtained from the EM counterpart with a waveform template that includes the birefringence parameter $\tilde{\kappa}$, one could estimate $\tilde{\kappa}$ and place bounds on amplitude birefringence. This bound could then be used to constrain alternative gravity theories.

Observation of a strong GW signal and an EM counterpart from a real NSBH coalescence, where the sky location and distance can be tightly constrained electromagnetically, would allow for strong bounds to be placed on amplitude birefringence.

A different experimental verification of amplitude birefringence is proposed by [4]. The effect of amplitude birefringence on the long GW signals of cosmologically distant inspiraling massive BBH systems, that will be observed with the space based GW detector LISA, would be an apparent time dependent change in the inclination angle. Sufficiently long observations of such a binary system will enable this apparent rotation to be distinguishable from precession.

A Spherical harmonic decomposition of the gravitational-wave polarizations

In GW theory, it is efficient to work with the complex valued quantity $h = h_+ - ih_\times$, a combination of the two polarizations of gravitational-waves h_+ and $h_\times$. From the perspective of an observer, h can be expanded into multipole moments using spherical polar coordinates. The -2 spin-weighted spherical harmonics ${}_{-2}Y_{lm}$ are the simplest appropriate harmonic basis [46]. In this basis, the multipolar decomposition can be written as [61]

$$h_+ - ih_\times = \sum_{l\geq 2} \sum_{m=-l}^{l} {}_{-2}Y_{lm}(\iota, \phi_c)\ h_{lm}, \tag{A.1}$$

where the coefficients h_{lm} are the radiative multipoles depending on the source properties and ϕ_c is the coalescence phase. For non-precessing binaries, $\tilde{h}_+$ and $\tilde{h}_\times$ can be expressed in the Fourier domain, where gravitational-wave data analysis is usually done, as[1]

$$\begin{aligned}
\tilde{h}_+(f) &= \frac{1}{2}\sum_{l\geq 2} \sum_{m=-l}^{l} \left[{}_{-2}Y_{lm}(\iota, \phi_c)\ \tilde{h}_{lm}(f) + {}_{-2}Y^*_{lm}(\iota, \phi_c)\ \tilde{h}_{lm}(-f)^* \right] \\
&= \frac{1}{2}\sum_{l\geq 2} \sum_{m=1}^{l} \left[{}_{-2}Y_{lm}(\iota, \phi_c) + (-1)^l {}_{-2}Y^*_{l-m}(\iota, \phi_c) \right]\ \tilde{h}_{lm}(f) \\
\tilde{h}_\times(f) &= \frac{i}{2}\sum_{l\geq 2} \sum_{m=-l}^{l} \left[{}_{-2}Y_{lm}(\iota, \phi_c)\ \tilde{h}_{lm}(f) - {}_{-2}Y^*_{lm}(\iota, \phi_c)\ \tilde{h}_{lm}(-f)^* \right] \\
&= \frac{i}{2}\sum_{l\geq 2} \sum_{m=1}^{l} \left[{}_{-2}Y_{lm}(\iota, \phi_c) - (-1)^l {}_{-2}Y^*_{l-m}(\iota, \phi_c) \right]\ \tilde{h}_{lm}(f).
\end{aligned} \tag{A.2}$$

The spherical harmonics for the dominant $(2, \pm 2)$ modes are

$$\begin{aligned}
{}_{-2}Y_{22} &= \frac{1}{2}\sqrt{\frac{5}{\pi}} e^{2i\phi_c} \cos^4\left(\frac{\iota}{2}\right) \\
{}_{-2}Y_{2-2} &= \frac{1}{2}\sqrt{\frac{5}{\pi}} e^{-2i\phi_c} \sin^4\left(\frac{\iota}{2}\right).
\end{aligned} \tag{A.3}$$

With these expressions and using the formulas [62]

$$\sin\left(\frac{x}{2}\right) = \pm\sqrt{\frac{1-\cos x}{2}} \qquad \text{and} \qquad \cos\left(\frac{x}{2}\right) = \pm\sqrt{\frac{1+\cos x}{2}} \tag{A.4}$$

one finds that for the dominant mode

[1] For a more detailed discussion see Appendix A of [61].

$$\begin{aligned}\tilde{h}_+(f) &= \frac{1}{4}\sqrt{\frac{5}{\pi}}e^{2i\phi_c}\frac{1}{2}(1+\cos^2\iota)\ \tilde{h}_{22}(f)\\ \tilde{h}_\times(f) &= \frac{i}{4}\sqrt{\frac{5}{\pi}}e^{2i\phi_c}\cos\iota\ \tilde{h}_{22}(f).\end{aligned} \tag{A.5}$$

Simple general expressions for $\tilde{h}_+$ and $\tilde{h}_\times$ for non-precessing binaries are given by [61] as

$$\begin{aligned}\tilde{h}_+ &= \frac{d_o}{d_L}\sum_{l\geq 2}\sum_{m=0}^{l}A_+^{lm}(\iota)e^{im\phi_c}\tilde{h}_{lm}(f)\\ \tilde{h}_\times &= \frac{d_o}{d_L}\sum_{l\geq 2}\sum_{m=0}^{l}A_\times^{lm}(\iota)ie^{im\phi_c}\tilde{h}_{lm}(f),\end{aligned} \tag{A.6}$$

where d_o is a distance used to normalize the waveforms $\tilde{h}_{lm}$. The amplitudes A^{lm} are functions only of the inclination angle. For the most significant harmonics, they are given as [61]

$$\begin{aligned}A_+^{22} &= \frac{1}{2}(1+\cos^2\iota)\\ A_\times^{22} &= \cos\iota\\ A_+^{21} &= \sin\iota\\ A_\times^{21} &= \sin\iota\cos\iota\\ A_+^{33} &= \sin\iota\ (1+\cos^2\iota)\\ A_\times^{33} &= 2\sin\iota\cos\iota\\ A_+^{44} &= \sin^2\iota\ (1+\cos^2\iota)\\ A_\times^{44} &= 2\sin^2\iota\cos\iota.\end{aligned} \tag{A.7}$$

There is a freedom to choose an overall normalization for these amplitudes, which corresponds to an overall rescaling of the waveform $\tilde{h}_{lm}$. It is customary to choose a normalization such that $A_+^{22} = A_\times^{22} = 1$ for face-on systems, when $\iota = 0$. This is the normalization used here, which is different from the convention used before.

It is straight forward to see that for the dominant harmonic ($l = 2, m = \pm 2$) we can write [63, 64]

$$\begin{aligned}\tilde{h}_+ &= \frac{1}{2}(1+\cos^2\iota)\mathcal{A}e^{i\Psi}\\ \tilde{h}_\times &= \cos\iota\ \mathcal{A}ie^{i\Psi} = \cos\iota\ \mathcal{A}e^{i(\Psi+\pi/2)}\end{aligned} \tag{A.8}$$

with an amplitude $\mathcal{A}$ and phase Ψ, which is consistent with Equation (A.5). A derivation of h_+ and $h_\times$ for a quadrupole source is given e.g. in [65].

Using these expressions in $h_R = (h_+ - ih_\times)/\sqrt{2}$ and $h_L = (h_+ + ih_\times)/\sqrt{2}$ one can easily derive Equation (2.3)

$$\frac{h_R}{h_L} = \frac{h_+ - ih_\times}{h_+ + ih_\times} = \frac{(1+\cos\iota)^2}{(1-\cos\iota)^2}. \tag{A.9}$$

This result applies also for all higher harmonics with $l = |m|$ as can be seen from the amplitudes A^{ll} given in Equation (A.7). For the sum over all modes with $l = m$ in Equation (A.6), we obtain

$$\begin{aligned}\tilde{h}_+ &= \frac{d_o}{d_L}\ \frac{1}{2}(1+\cos^2\iota)\left[e^{i2\phi_c}\tilde{h}_{22} + 2\sin\iota\ e^{i3\phi_c}\tilde{h}_{33} + 2\sin^2\iota\ e^{i4\phi_c}\tilde{h}_{44} + ...\right] \\ \tilde{h}_\times &= \frac{d_o}{d_L}\ \cos\iota\ i\left[e^{i2\phi_c}\tilde{h}_{22} + 2\sin\iota\ e^{i3\phi_c}\tilde{h}_{33} + 2\sin^2\iota\ e^{i4\phi_c}\tilde{h}_{44} + ...\right],\end{aligned} \tag{A.10}$$

where the terms in square brackets are the same for both polarizations and the usual dependence on ι seen for the dominant mode in Equation (A.8) factors out. Thus, when evaluating Equation (A.9) the terms in the square brackets cancel and we obtain the simple dependence on $\cos\iota$.

Bibliography

[1] B. Abbott *et al.*, "Observation of gravitational waves from a binary black hole merger," *Physical Review Letters* **116** no. 6, (2016) , arXiv:1602.03837.

[2] B. Abbott *et al.*, "Tests of general relativity with the binary black hole signals from the LIGO-Virgo catalog GWTC-1," *Physical Review D* **100** no. 10, (2019) , arXiv:1903.04467.

[3] B. Abbott *et al.*, "Tests of general relativity with GW170817," *Physical Review Letters* **123** no. 1, (2019) , arXiv:1811.00364.

[4] S. Alexander, L. S. Finn, and N. Yunes, "Gravitational-wave probe of effective quantum gravity," *Physical Review D* **78** no. 6, (2008) , arXiv:0712.2542.

[5] Y.-F. Wang, R. Niu, T. Zhu, and W. Zhao, "Gravitational wave implications for the parity symmetry of gravity in the high energy region," *The Astrophysical Journal* **908** no. 1, (2021) 58, arXiv:2002.05668.

[6] T. D. Lee and C. N. Yang, "Question of parity conservation in weak interactions," *Phys. Rev.* **104** (1956) 254–258.

[7] C. S. Wu, E. Ambler, R. W. Hayward, D. D. Hoppes, and R. P. Hudson, "Experimental test of parity conservation in beta decay," *Phys. Rev.* **105** (1957) 1413–1415.

[8] S. Alexander and N. Yunes, "Chern–Simons modified general relativity," *Physics Reports* **480** no. 1-2, (2009) 1–55, arXiv:0907.2562.

[9] K. Yagi and H. Yang, "Probing gravitational parity violation with gravitational waves from stellar-mass black hole binaries," *Physical Review D* **97** no. 10, (2018) , arXiv:1712.00682.

[10] S. H. Alexander and N. Yunes, "Gravitational wave probes of parity violation in compact binary coalescences," *Physical Review D* **97** no. 6, (2018) , arXiv:1712.01853.

[11] W. Zhao, T. Zhu, J. Qiao, and A. Wang, "Waveform of gravitational waves in the general parity-violating gravities," *Physical Review D* **101** no. 2, (2020) 024002, arXiv:1909.10887.

[12] J. Qiao, T. Zhu, W. Zhao, and A. Wang, "Waveform of gravitational waves in the ghost-free parity-violating gravities," *Physical Review D* **100** no. 12, (2019) , arXiv:1909.03815.

[13] N. Seto and A. Taruya, "Polarization analysis of gravitational-wave backgrounds from the correlation signals of ground-based interferometers: Measuring a circular-polarization mode," *Physical Review D* **77** no. 10, (2008) , arXiv:0801.4185.

[14] S. Mirshekari, N. Yunes, and C. M. Will, "Constraining lorentz-violating, modified dispersion relations with gravitational waves," *Physical Review D* **85** no. 2, (2012) , arXiv:1909.03815.

[15] R. Jackiw and S.-Y. Pi, "Chern-Simons modification of general relativity," *Physical Review D* **68** no. 10, (2003) , arXiv:0308071.

[16] M. Okounkova, W. M. Farr, M. Isi, and L. C. Stein, "Constraining gravitational wave amplitude birefringence and Chern-Simons gravity with GWTC-2," *ArXiv e-prints* (2021) , arXiv:2101.11153.

[17] O. Piattella, "Lecture notes in cosmology," *UNITEXT for Physics* (2018) , arXiv:1803.00070.

[18] S. M. Carroll, *Spacetime and Geometry: An Introduction to General Relativity*. Cambridge University Press, 2019.

[19] K. Hotokezaka, E. Nakar, O. Gottlieb, S. Nissanke, K. Masuda, G. Hallinan, K. P. Mooley, and A. T. Deller, "A Hubble constant measurement from superluminal motion of the jet in GW170817," *ArXiv e-prints* (2018) , arXiv:1806.10596.

[20] E. Nakar and T. Piran, "Afterglow constraints on the viewing angle of binary neutron star mergers and determination of the Hubble constant," *ArXiv e-prints* (2021) , arXiv:2005.01754.

[21] E. Nakar, "The electromagnetic counterparts of compact binary mergers," *Physics Reports* **886** (2020) 1–84, arXiv:1912.05659.

[22] E. Berger, "Short-duration gamma-ray bursts," *Annual Review of Astronomy and Astrophysics* **52** no. 1, (2014) 43–105, arXiv:1311.2603.

[23] A. Levan, P. Crowther, R. de Grijs, N. Langer, D. Xu, and S.-C. Yoon, "Gamma-ray burst progenitors," *Space Science Reviews* **202** no. 1-4, (2016) 33–78, arXiv:1611.03091.

[24] K. P. Mooley, A. T. Deller, O. Gottlieb, E. Nakar, G. Hallinan, S. Bourke, D. A. Frail, A. Horesh, A. Corsi, and K. Hotokezaka, "Superluminal motion of a relativistic jet in the neutron-star merger GW170817," *Nature* **561** no. 7723, (2018) 355–359, arXiv:1806.09693.

[25] O. S. Salafia, G. Ghisellini, A. Pescalli, G. Ghirlanda, and F. Nappo, "Structure of gamma-ray burst jets: intrinsic versus apparent properties," *Monthly Notices of the Royal Astronomical Society* **450** no. 4, (2015) 3549–3558, arXiv:1502.06608.

[26] P. Beniamini, M. Petropoulou, R. Barniol Duran, and D. Giannios, "A lesson from GW170817: most neutron star mergers result in tightly collimated successful GRB jets," *Monthly Notices of the Royal Astronomical Society* **483** no. 1, (2018) 840–851, arXiv:1808.04831.

[27] C. Barbieri, O. S. Salafia, A. Perego, M. Colpi, and G. Ghirlanda, "Electromagnetic counterparts of black hole–neutron star mergers: dependence on the neutron star properties," *The European Physical Journal A* **56** no. 1, (2020) , arXiv:1908.08822.

[28] C. Barbieri, O. S. Salafia, A. Perego, M. Colpi, and G. Ghirlanda, "Light-curve models of black hole – neutron star mergers: steps towards a multi-messenger parameter estimation," *Astronomy and Astrophysics* **625** (2019) A152, arXiv:1903.04543.

[29] F. Foucart, "A brief overview of black hole-neutron star mergers," *Frontiers in Astronomy and Space Sciences* **7** (2020) , arXiv:2006.10570.

[30] A. W. Steiner, M. Hempel, and T. Fischer, "Core-collapse supernova equations of state based on neutron star observations," *The Astrophysical Journal* **774** no. 1, (2013) 17, arXiv:1207.2184.

[31] B. Abbott *et al.*, "GW170817: Measurements of neutron star radii and equation of state," *Physical Review Letters* **121** no. 16, (2018) , arXiv:1805.11581.

[32] A. Kathirgamaraju, A. Tchekhovskoy, D. Giannios, and R. Barniol Duran, "EM counterparts of structured jets from 3D GRMHD simulations," *Monthly Notices of the Royal Astronomical Society: Letters* **484** no. 1, (2019) L98–L103, arXiv:1809.05099.

[33] W. Fong, E. Berger, R. Margutti, and B. A. Zauderer, "A decade of short-duration gamma-ray burst broadband afterglows: Energetics, circumburst densities, and jet opening angles," *The Astrophysical Journal* **815** no. 2, (2015) 102, arXiv:1509.02922.

[34] O. Gottlieb, E. Nakar, and T. Piran, "Detectability of neutron star merger afterglows," *Monthly Notices of the Royal Astronomical Society* **488** no. 2, (2019) 2405–2411, arXiv:1903.08173.

[35] M. Tanaka, K. Hotokezaka, K. Kyutoku, S. Wanajo, K. Kiuchi, Y. Sekiguchi, and M. Shibata, "Radioactively powered emission from black hole-neutron star mergers," *The Astrophysical Journal* **780** no. 1, (2013) 31, arXiv:1310.2774.

[36] E. Nakar, T. Piran, and J. Granot, "The detectability of orphan afterglows," *The Astrophysical Journal* **579** no. 2, (2002) 699–705, arXiv:0204203.

[37] R. Sari, T. Piran, and R. Narayan, "Spectra and light curves of gamma-ray burst afterglows," *The Astrophysical Journal* **497** no. 1, (1998) L17–L20, arXiv:9712005.

[38] L. Sironi, A. Spitkovsky, and J. Arons, "The maximum energy of accelerated particles in relativistic collisionless shocks," *The Astrophysical Journal* **771** no. 1, (2013) 54, arXiv:1301.5333.

[39] P. Beniamini and A. J. van der Horst, "Electrons' energy in GRB afterglows implied by radio peaks," *Monthly Notices of the Royal Astronomical Society* **472** no. 3, (2017) 3161–3168, arXiv:1706.07817.

[40] P. Beniamini, L. Nava, and T. Piran, "A revised analysis of gamma-ray bursts' prompt efficiencies," *Monthly Notices of the Royal Astronomical Society* **461** no. 1, (2016) 51–59, arXiv:1606.00311.

[41] B. F. Schutz, "Networks of gravitational wave detectors and three figures of merit," *Classical and Quantum Gravity* **28** no. 12, (2011) 125023, arXiv:1102.5421.

[42] H.-Y. Chen, D. E. Holz, J. Miller, M. Evans, S. Vitale, and J. Creighton, "Distance measures in gravitational-wave astrophysics and cosmology," *Classical and Quantum Gravity* **38** no. 5, (2021) 055010, arXiv:1709.08079.

[43] B. P. Abbott *et al.*, "Prospects for observing and localizing gravitational-wave transients with Advanced LIGO, Advanced Virgo and KAGRA," *Living Reviews in Relativity* **23** no. 1, (2020) , arXiv:1304.0670.

[44] K. G. Arun, H. Tagoshi, A. Pai, and C. K. Mishra, "Synergy of short gamma ray burst and gravitational wave observations: Constraining the inclination angle of the binary and possible implications for off-axis gamma ray bursts," *Physical Review D* **90** no. 2, (2014) 024060, arXiv:1403.6917.

[45] H.-Y. Chen, S. Vitale, and R. Narayan, "Viewing angle of binary neutron star mergers," *Physical Review X* **9** no. 3, (2019) 031028, arXiv:1807.05226.

[46] R. Abbott *et al.*, "GW190412: Observation of a binary-black-hole coalescence with asymmetric masses," *Physical Review D* **102** no. 4, (2020) 043015, arXiv:2004.08342.

[47] J. D. E. Creighton and W. G. Anderson, *Gravitational-wave physics and astronomy: An introduction to theory, experiment and data analysis*. Wiley-VCH Verlag GmbH and Co. KGaA, Weinheim, 2011.

[48] G. E. P. Box and G. C. Tiao, *Bayesian inference in statistical analysis*. John Wiley and Sons, New York, 1992.

[49] C. Cutler and E. E. Flanagan, "Gravitational waves from merging compact binaries: How accurately can one extract the binary's parameters from the inspiral waveform?" *Physical Review D* **49** no. 6, (1994) 2658–2697, arXiv:9402014.

[50] L. A. Wainstein and V. D. Zubakov, *Extraction of signals from noise*. Dover Publications, New York, 1970.

[51] R. Abbott *et al.*, "Observation of gravitational waves from two neutron star–black hole coalescences," *The Astrophysical Journal Letters* **915** no. 1, (2021) L5, arXiv:2106.15163.

[52] "LIGO document control center portal," 10.3.2021. https://dcc.ligo.org/LIGO-P190412/public.

[53] B. Abbott *et al.*, "GWTC-1: A gravitational-wave transient catalog of compact binary mergers observed by LIGO and Virgo during the first and second observing runs," *Physical Review X* **9** no. 3, (2019) , arXiv:1811.12907.

[54] B. P. Abbott *et al.*, "GW170817: Observation of gravitational waves from a binary neutron star inspiral," *Physical Review Letters* **119** no. 16, (2017) 161101, arXiv:1710.05832.

[55] M. Soares-Santos *et al.*, "The electromagnetic counterpart of the binary neutron star merger LIGO/Virgo GW170817. I. discovery of the optical counterpart using the dark energy camera," *The Astrophysical Journal* **848** no. 2, (2017) L16, arXiv:1710.05459.

[56] M. Cantiello *et al.*, "A precise distance to the host galaxy of the binary neutron star merger GW170817 using surface brightness fluctuations," *The Astrophysical Journal* **854** no. 2, (2018) L31, arXiv:1801.06080.

[57] D. Finstad, S. De, D. A. Brown, E. Berger, and C. M. Biwer, "Measuring the viewing angle of GW170817 with electromagnetic and gravitational waves," *The Astrophysical Journal* **860** no. 1, (2018) L2, arXiv:1804.04179.

[58] B. Abbott *et al.*, "Properties of the binary neutron star merger GW170817," *Physical Review X* **9** no. 1, (2019) , arXiv:1805.11579.

[59] M. Vallisneri, "Use and abuse of the fisher information matrix in the assessment of gravitational-wave parameter-estimation prospects," *Physical Review D* **77** no. 4, (2008) , arXiv:0703086.

[60] P. A. R. Ade *et al.*, "Planck 2015 results," *Astronomy and Astrophysics* **594** (2016) A13, arXiv:1502.01589.

[61] C. Mills and S. Fairhurst, "Measuring gravitational-wave higher-order multipoles," *Physical Review D* **103** no. 2, (2021) , arXiv:2007.04313.

[62] L. Papula, *Mathematische Formelsammlung.* Vieweg+Teubner, Wiesbaden, 2009.

[63] B. S. Sathyaprakash and B. F. Schutz, "Physics, astrophysics and cosmology with gravitational waves," *Living Reviews in Relativity* **12** no. 1, (2009) , arXiv:0903.0338.

[64] M. Maggiore, *Gravitational Waves. Vol. 1: Theory and Experiments.* Oxford University Press, Oxford, 2007.

[65] J. T. Whelan, "The geometry of gravitational wave detection," July 4th, 2013 [PDF]. https://dcc.ligo.org/public/0106/T1300666/003/Whelan_geometry.pdf.